Department of Chemistry, University of Jyväskylä

SPECTROSCOPIC STUDIES OF ATOMS AND SMALL MOLECULES ISOLATED IN RARE GAS SOLIDS: PHOTODISSOCIATION AND THERMAL REACTIONS

JUSSI AHOKAS

Academic Dissertation
for the Degree of
Doctor of Philosophy

Jyväskylä, Finland 2006

Research Report No. 117

DEPARTMENT OF CHEMISTRY, UNIVERSITY OF JYVÄSKYLÄ
RESEARCH REPORT No. 117

SPECTROSCOPIC STUDIES OF ATOMS AND SMALL MOLECULES ISOLATED IN RARE GAS SOLIDS: PHOTODISSOCIATION AND THERMAL REACTIONS

BY

JUSSI AHOKAS

Academic Dissertation
for the degree of
Doctor of Philosophy

To be presented, by permission of the Faculty of Mathematics and Science of the University of Jyväskylä, for public examination in Auditorium KEM1, on 17th November 2006, at 12 noon

Jyväskylä, Finland
ISBN 951-39-2602-8
ISSN 0357-346X

URN:ISBN:978-951-39-9858-5
ISBN 978-951-39-9858-5 (PDF)
ISSN 0357-346X

Jyväskylän yliopisto, 2023

Preface

This work has been carried out between the years 2000 and 2006 at the Department of Chemistry, University of Jyväskylä.

I would like to express my warmest gratitude to my patient supervisor Prof. Henrik Kunttu for giving me the opportunity to carry out this work. I am also thankful to him for giving me the opportunity to be involved in educational duties during these years.

I wish to thank Prof. Jussi Eloranta, Dr. Kari Vaskonen, and Dr. Toni Kiljunen for introducing me to the field of matrix isolation. I appreciate their help in the laboratory and with computational problems. Inspiring discussions with them have been very helpful in my work. I also wish to thank Dr. Mika Pettersson for discussions during his time in Jyväskylä. Prof. Markku Räsänen and Dr. Leonid Khriachtchev are kindly thanked for their co-operation. I would also like to thank Dr. Evgeni Popov for guiding me in Moscow, in Chernogolovka, and in the field of superfluid helium.

Now, it is time to thank all of those who have shared the space of the coffee room with me during these years. Intellectual and, especially, non-intellectual discussions with you have delighted my days. And a word of thanks to the people from the whole Department of Chemistry. Their co-operation has been fruitful.

Professor Emeritus Matti Nurmia is thanked for revising the language of this thesis.

I wish to express my sincere thanks to my parents, parents-in-law, and friends for their support throughout my studies.

I dedicate my deepest gratitude to my family, Sanna, Venla, and Otso, who have supported me during this work.

Jyväskylä, August 2006

Jussi Ahokas

Abstract

The spectroscopy and the chemical dynamics of atoms and small molecules in solid rare gas matrices are studied in this thesis. The many-body nature of the surrounding solid environment causes effects on the spectroscopy and chemistry of the species embedded in the solid environment. These effects may lead to very different behaviour than expected according to the gas phase results. For example, the reaction between two thermally mobilized hydrogen atoms in solid xenon is hindered by an energy barrier, and reaction products other than molecular hydrogen are favored. Not only the reactions between atoms or molecules, but also their photochemistry is greatly affected by the solid surrounding.

The first half of the present thesis summarizes the studies of the novel rare gas compounds and the second half is dedicated to the studies of formyl fluoride and its dimers.

The electronic absorption spectra of the thermal reaction product molecules HXeY (Y = Cl, Br, I, CN, SH, OH, or H) were measured in solid xenon. A broad and structureless UV absorption is characteristic of these molecules. Quantum chemical calculations were carried out in order to support the spectral assignments. A kinetic model was used to simulate the reactions of thermally mobilized hydrogen atoms. The experimental evidence and computational predictions of the $HXeSH\cdots H_2S$ complex are also discussed.

The studies of formyl fluoride were focused on its photodissociation and dimerization. Four stable dimer structures were found computationally, and an experimentally observed blue shifted C–H stretching vibration was assigned to a formyl fluoride dimer containing a double –CH—O– hydrogen bond. The photodissociation of formyl fluoride is affected by the cage effect of the surrounding solid. This effect prevents the separation of the photoproducts and thus in-cage dynamics dominates. In-cage reactions yielded mainly molecular complexes between CO and HF. Computational predictions were made to rationalize the observed photodissociation of the complexes between CO and HF in solid krypton and xenon.

List of original publications

The main results of this thesis are presented in the following original research papers, which will be referred to in the text by their Roman numerals.

I **Electronic Absorption Spectra of HXeCl, HXeBr, HXeI and HXeCN in Xe Matrix**
Jussi Ahokas, Kari Vaskonen, Jussi Eloranta, and Henrik Kunttu
Journal of Physical Chemistry A **2000**, 104, 9506–9511.
https://doi.org/10.1021/jp002141t

II **UV Photolysis and Thermal Annealing of H_2S, HI, and H_2CO in solid Xe: Electronic Absorption Spectra of the Products**
Jussi Ahokas, Henrik Kunttu, Leonid Khriachtchev, Mika Pettersson, and Markku Räsänen
Journal of Physical Chemistry A **2002**, 106, 7743–7747.
https://doi.org/10.1021/jp0259824

III **Photodissociation of Formyl Fluoride in Rare Gas Matrices**
Jussi Ahokas, Kari Vaskonen, and Henrik Kunttu
Journal of Physical Chemistry A **2006**, 110, 6208–6215.
https://doi.org/10.1021/jp060249o

IV **Structure and Matrix Isolation Infrared Spectrum of Formyl Fluoride Dimer: Blue-Shift of the C–H Stretching Frequency**
Jussi Ahokas, Kari Vaskonen, and Henrik Kunttu
Journal of Physical Chemsitry A **2006**, 110, 7816–7821.
https://doi.org/10.1021/jp061188x

The author of the present thesis has done most of the experimental work and analysed the results in publications I and II. The author has done all the experimental and computational work reported in Papers III and IV, and he has also written those papers.

Contents

Preface iv

Abstract vi

List of original publications viii

1 Introduction 1
- 1.1 Matrix isolation 1
- 1.2 Dynamics of Photodissociation . 3
  - 1.2.1 Matrix cage effect 3
- 1.3 Rare gas chemistry in rare gas matrices . 5
- 1.4 Complexes in rare gas matrices . . . 7
  - 1.4.1 Hydrogen bonded complexes . . . 7

2 Methods 9
- 2.1 Experimental methods 9
- 2.2 Computational methods 10

3 Results and discussion 13
- 3.1 Novel rare gas compounds 13
  - 3.1.1 Electronic absorption spectra 13
  - 3.1.2 On the formation and decomposition mechanisms 18
  - 3.1.3 Comment on the usability of the UV absorption technique 22
  - 3.1.4 Does HXeSH$\cdots$$H_2S$ exist? 23
- 3.2 Formyl fluoride 28
  - 3.2.1 Infrared spectrum of HCOF and HCOF dimer 28
  - 3.2.2 Structure of the HCOF dimer . . . 31
  - 3.2.3 Photodissociation of formyl fluoride 35

4 Conclusions 43

References **46**

Chapter 1

Introduction

This thesis summarizes the results of four articles included at the end of the thesis and referred to as Papers I, II, III, and IV. The published articles cover three different topics. The connecting link between these studies is the chemical kinetics of small molecules in solid rare gas matrices, and matrix isolation combined with optical spectroscopy has been utilized throughout the studies.

Electronic absorption spectra of novel rare gas compounds were studied in Papers I and II. The photodissociation of formyl fluoride in rare gas matrices was studied in Paper III, while the structure and the infrared spectrum of formyl fluoride dimer were studied in Paper IV.

Some previously unpublished results have been included in the following discussion, in order to deepen the current understanding of the topic. Next, a brief introduction to current topics and the methods used is given, and then the results from Papers I–IV are presented and discussed.

1.1 Matrix isolation

Matrix isolation (MI) is an experimental method, which was initially developed to provide experimental conditions for spectroscopic studies of reactive and unstable species [1]. The basic idea of this method is to preserve the compound under interest (guest) in a solid medium (host). Typically, a large excess of the host is used to ensure that the quests are surrounded by the host only. In the solid environment the guest species are prevented from diffusion and are therefore prevented from undergoing bimolecular reactions, except with the host. In other words, the trapped guest species are caged by the surrounding host atoms [2, 3].

Practically, experimentalists are often urged to find systems where the

guest-to-host interactions are as weak as possible, so that the properties of the species under interest are not significantly changed by this interaction. In order to provide a weak guest-to-host interaction, inert hosts, such as rare gases from neon to xenon or nitrogen, are frequently used. The solidification of rare gases or nitrogen requires low temperatures; typically 6 - 70 K are required. These hosts have the advantages of being transparent throughout the UV–visible and the mid-IR region [2, 3]. This is an obvious and necessary requirement for the utilization of optical spectroscopy. In addition to optical spectroscopy, magnetic spectroscopy can be also used with the matrix isolation technique [2, 4]. Reactive hosts are sometimes used to study reactions between the host and the guest or species generated within the matrix [2].

Rare gas solids possess a cubic closed-packed structure with a face centered cubic (FCC) unit cell. The guests are trapped in rare gas solids in well defined trapping sites, the size and geometry of which are dictated by the chemical nature and geometry of the guests and the host. Three different trapping sites, substitutional, interstitial, and defect sites, are often assumed to be available to trapped atoms and molecules. A substitutional site is formed when one or more host atoms are replaced by the trapped species. In interstitial trapping the guest is located at an octahedral or tetrahedral site. The short nearest neighbor distance in octahedral sites favors trapping of single atoms, or small molecules such as hydrogen fluoride, at these sites. Since the commonly used methods to grow solid matrices produce more or less ideal crystals, the defect sites are also possible trapping sites. However, very sharp vibrational bands of trapped molecules can be regarded as evidence for well-defined trapping sites. Typically the size and the geometry of the trapping site prevents molecular rotation, except for small molecules, where only the lowest rotational states are populated at low temperatures [3, 5].

1.2 Dynamics of Photodissociation

The photon-induced dissociation of a single small molecule in the gas phase can be initiated by a direct electronic excitation onto a dissociative potential energy surface (PES), where dissociation takes place. Alternatively, dissociation may proceed via a bound electronically excited state (predissociative state), if there exist an intersection between the bound and dissociative PESs, or if there exists a region of avoided crossing of two PESs [6]. If molecular impurities are embedded in a solid environment, more processes have to be considered. The electronic excitation of the host itself or a guest–host pair may be followed by photodissociation of a molecular impurity [7]. An electronic exitation of a solid xenon host to excitonic bands and subsequent trapping of free excitons into the molecular site have been characterized as a dissociation mechanism of N_2O in a xenon matrix [8]. Harpoon reactions are well studied examples of molecular photodissociation initiated by the excitation of a guest–host intermolecular charge-transfer transition in a solid xenon matrix [9–11]. A photochemically induced intermolecular electronic energy transfer of geminate guests can also provide a photodissociation pathway for molecular guests [12].

Although a molecule is excited above its dissociation limit in a solid matrix and dissociation is assumed to take place, the matrix cage effect has a substantial effect on the photodissociation dynamics of a molecule [7]. Hence, the matrix cage effect has to be considered when photodissociation dynamics of trapped molecules is studied.

1.2.1 Matrix cage effect

The matrix cage effect arises from the rigidity of the low-temperature matrix, and it influences the reaction pathway. The cage effect can be understood as a potential barrier around the trapped species formed by the surrounding host atoms. When two species are generated in a matrix cage by photodissociation, the new species have the possibility to leave the cage, react in the cage, or stay in the cage unreacted [7, 13]. Photodissociation consumes a portion of the energy of the photon, and the difference between the dissociation energy and the photon energy is called the excess energy. The excess energy is shared between the fragments and it is distributed among electronic, kinetic, vibrational, and rotational degrees of freedom after the photodissociation. If the species have enough excess energy after the photodissociation, there are generally two mechanisms for the cage exit, *i.e.* the permanent separation of the photochemically generated species. If a species has enough kinetic energy it can blast out from the cage, either directly by displacing host atoms

or through an area of low energy barrier, a cage window. Alternatively, the kinetic energy can be used to distort the surrounding cage and to open a new cage window, a region of lower potential barrier. Two direct cage exit mechanisms are referred to forced and sudden, respectively, while the latter is delayed [7]. An excess energy above 4 eV is needed for forced cage exit, while an excess energy of ~1.8 eV is sufficient for sudden cage exit of hydrogen atoms in argon and krypton matrices. A delayed cage exit of hydrogen atom is considered to happen at excess energies below 1.7 eV. In a xenon matrix the cage exit of hydrogen atoms takes place at an excess energy of ~1.3 eV [7, 14–16].

1.3 Rare gas chemistry in rare gas matrices

Rare gases are often considered as inert in general text books, although their capability to form chemical bonds with other elements was well demonstrated during the last century [17]. A new era started for rare gases in 1962, when Bartlett introduced the first stable rare gas containing compound $XePtF_6$ [18, 19]. After Bartlett's successful experiment, an entire family of rare gas containing compounds has been introduced, not only in the gas and liquid phases, but also in low temperature matrices [17].

In this thesis, the main interest is focused on novel rare gas compounds in rare gas matrices. A good introduction to this issue can be found in the recent reviews of Refs. [20], [21], and [22]. The pioneering experiments in this field have been carried out in Helsinki by the Räsänen group, which for the first time characterized the novel rare gas containing molecules of type HRgY (or DRgY), where Rg was krypton or xenon and Y typically an electronegative atom or molecular fragment, such as Cl, Br, I, CN, SH, or OH, in low temperature rare gas matrices [23–26]. As distinct from a typical form of HRgY, where Y is electronegative, two hydrogen atoms can react with a xenon atom and form the HXeH molecule [27].

Since the discovery of HRgY type molecules, a number of low temperature molecules containing xenon and krypton, including so called organoxenon compounds, such as HXeCCH [28], have been prepared and characterized in rare gas matrices [22]. Subsequent studies in argon matrix revealed the chemical activity of argon atoms; the first chemically bound argon compound, HArF, was observed by the Räsänen group [29]. A more extreme breakdown of chemical inertness was theoretically established when the HHeF molecule was predicted to be metastable [30–32]. HHeF is excepted to remain stable in solid helium at pressures well above 23 GPa [33], and its stabilization by complexation with Xe atoms has been discussed later [34].

The preparation of novel rare gas molecules is related to photodissociation of a suitable precursor molecule in a suitable matrix, for example hydrogen halides in a xenon matrix [22]. The photodissociation leads to a separation of hydrogen and halogen atoms as long as the temperature is kept below the thermal mobilization temperature of hydrogen atoms in solid xenon. When the temperature is raised to ca. 45 K, hydrogen atoms become thermally mobile in solid xenon [35 39]. The mobile hydrogen atoms can then attack the Xe end of the XeY pair (Y = *e.g.* halogen or hydrogen) and form a HXeY compound.

A general feature of the rare gas molecules is their structure of form HRgY (Rg = Ar, Kr, or Xe), where Y is an electronegative atom or hydrogen atom, a molecular fragment such as CN radical, or a hydrocarbon radical such

as CCH in the HXeCCH molecule [22]. The bonding in HRgY is ionic, and can be described as $(HRg)^+Y^-$, where Y has a negative partial charge and the covalently bound HRg fragment has a positive partial charge. The interaction between HRg^+ and Y^- is mainly Coulombic attraction [23, 27, 40, 41]. Since the HRgY rare gas molecules have extremely intense IR absorptions of the H–Rg stretching mode, the experimental observations of these molecules have been based on IR spectroscopy and supporting quantum chemical calculations [22].

1.4 Complexes in rare gas matrices

Besides isolated molecules, the trapped species in solid matrices can be molecular aggregates. The MI technique has been widely used to study the spectroscopic properties of such aggregates [2, 3, 5]. The advantage of MI is that the weak guest–host interactions make the guest–guest interactions more important. In fact, the weak guest–host interactions can be regarded as a weak solvent effect. In a solid matrix the vibrational bands of aggregates are substantially narrowed in contrast to the liguid phase; this makes the MI vibrational spectroscopy a superior technique. In contrast to the gas phase, the MI technique enables the use of low temperatures, which is necessary in the study of weak interactions. Many weakly bonded systems, including systems that are unstable at room temperatures, can be studied well in low temperature matrices. In this thesis, hydrogen-bonded formyl fluoride complexes were studied in Paper IV. The general features of hydrogen bonds are presented below.

1.4.1 Hydrogen bonded complexes

A hydrogen bond can be described as an interaction within a covalently bound X H pair, where X is electronegative relative to H, and Y, which possesses lone-pair electrons or polarizable π-electrons. Shortly, it is a bond between electron-deficient hydrogen and a region of high electron density of the form X–H$\cdots$Y [42]. Many complexes are often classified as van der Waals- or hydrogen-bonded, but this classification is not unambiguous, since hydrogen bonds resemble a wide variety of interactions. The strongest hydrogen bonds are mostly covalent, while weak hydrogen bonds are close to van der Waals binding.

A theoretical interpretation of a hydrogen bond can be realized as a sum of different contributions to the hydrogen bond wavefunction. First interpretions based on the valence bond theory and five contributions from the valence bond picture is adopted:

$$\begin{aligned}\Psi_{\mathrm{HB}} =& c_1\Psi^{(\mathrm{covalent})}_{\mathrm{X\text{–}H}} + c_2\Psi^{(\mathrm{ionic})}_{\mathrm{X^-\text{–}H^+}} + c_3\Psi^{(\mathrm{CT})}_{\mathrm{X^-\text{–}H\cdots Y^+}} \\ &+ c_4\Psi^{(\mathrm{ionic})}_{\mathrm{X^+\text{–}H^-}} + c_5\Psi^{(\mathrm{CT})}_{\mathrm{X\text{–}H^-\cdots Y^+}} \quad , \end{aligned} \tag{1.1}$$

where the contributions are covalent, ionic, and charge transfer (CT) and cofficients c_i are found by energy minimization. The electrostatic part of the wavefunction, $\Psi^{(\mathrm{ionic})}$, contains a large contribution to the hydrogen bond energy [42]. This idea of energy decomposition can be extended; in a widely used energy decomposition method the total intermolecular interaction en-

ergy is decomposed into electrostatic (ES), polarization (PL), exchange repulsion (EX), charge transfer (CT), and coupling terms (MIX) [43]:

$$E_{\mathrm{HB}} = E_{\mathrm{ES}} + E_{\mathrm{PL}} + E_{\mathrm{EX}} + E_{\mathrm{CT}} + E_{\mathrm{MIX}}. \tag{1.2}$$

The importance of each energy term depends on the type of the hydrogen bond. For strongly ionic hydrogen bonds the ES and CT terms are the most important ones; for moderately strong hydrogen bonds in which the proton donor and the proton acceptor are neutral ES is the most important term for the energy, while CT has a smaller contribution to the energy but a significant contribution to the electron distribution in the X–H region. The CT contribution comes mainly from a σ-type charge transfer from the proton acceptor (Y) to the proton donor (X–H). Polarization is the largest contributor to the charge redistribution in molecules.

The σ-type charge transfer from Y to X–H increases the electron density in the antibonding orbital of X–H, and is assumed to cause a weakening of the covalent X–H bond [44]. However, this is not a fully satisfactory explanation, because changes in the electron distribution in a single molecular orbital can be very small and yet cause a substantial charge transfer [45]. A weakening and concomitant lengthening of the bond leads to a red-shift of the X–H stretching vibration. For a long time this was considered as an exclusive property of the hydrogen bond, but nowdays a large number of hydrogen bonded complexes are known where the X H bond strengthens upon the hydrogen bond formation, while the stretching frequency is blue-shifted [44, 46]. Although there has been a debate about the origin of the blue-shift, it has been demostrated that there is no fundamental difference between hydrogen bonds showing blue- or red-shifts of the X–H stretching vibration [46].

Chapter 2

Methods

2.1 Experimental methods

The preparation of samples is relatively straightforward in the matrix isolation technique sample since the guests are typically volatile. Thus, the host and guest can be mixed in the gas phase using partial pressures to achieve the desired mole ratio between the host and guest gases. The mole ratio is called matrix ratio, and it was typically within the range (guest/host) 1/100 - 1/10000. The gas mixture was then deposited onto a low-temperature substrate to form a low-temperature matrix. In the present investigation, low-temperature substrates CsI, quartz and MgF_2 were used and the gas was condensed with a typical flow rate of 0.5–1.0 mmol/h. Typically, deposition temperatures between 10–55 K were used and maintained with a closed-cycle helium cryostat (APD Cryogenics, DE-202). The higher the deposition temperature, the better optical quality of matrix is achieved, but higher deposition temperatures favour the formation of multimers. Thus, a compromise between the deposition temperature and the optical quality is needed. A good optical quality is very essential for VUV, UV and VIS absorption measurements, because scattering of light is stronger at shorter wavelenghts. The reason why multimers are formed at higher temperatures is due to the softening of the matrix-material which allows the diffusion of the doped molecules, resulting in aggregation of these molecules.

Fourier-transform infrared (FTIR) spectroscopy and VUV–VIS absorption spectroscopy were combined with the MI technique in order to characterize atoms and molecules and their spectroscopy in rare gas matrices. The advantages of FTIR and VUV–VIS absorption methods are related to the softness of the methods and their synchronous use, which enables data collection from the same sample on the same experimental stage by both

methods. In this context the softness of a method means that the collection of spectroscopic information does not destroy the sample or affect its chemistry. The FTIR measurements were carried out with a Nicoled Magna 760 spectrometer equipped with a HgCdTe detector and a KBr beamsplitter. The spectral resolution was 0.125 or 0.5 cm^{-1}. UV(VUV)/VIS measuments were carried out with a simple setup composed of a light source (D_2-lamp (Cathodeon VO1 or Beckmann) or Xe-lamp (Oriel)), a spectrograph (Oriel MS125 or Acton SP150), and a CCD (Princeton Instruments) or ICCD (Acton) camera as a detector. Typically, the UV spectra were collected without any additional optics; if necessary, one collecting lens was used to focus the light to the spectrograph slit. ArF (Lambda Physik, Optex), KrF (Lambda Physik, Optex), and XeCl (Estonian Academy of Sciences, ELI94, ELI76E) excimer lasers and discharge lamps (Xe, D_2) were use to irradiate samples

2.2 Computational methods

Quantum chemical calculations were used in Papers I, III, and IV to describe the molecular properties and to support spectroscopic assignments. The geometries, vibrational properties, and excited states were computed by *ab initio* methods implemented in the Gaussian [47], MOLPRO [48], and GAMESS(US) [49] software packages. The methods used are well described in the literature, and a short description of the methods is given below [50, 51].

Quantum mechanics is needed, for describing the electronic structure of molecules in detail. Quantum mechanical methods are based on solving the time-independent Schrödinger equation

$$\widehat{H}\Psi(\mathbf{r};\mathbf{R}) = E\Psi(\mathbf{r};\mathbf{R}), \tag{2.1}$$

where $\widehat{H}$ is the Hamilton operator of the system, $\Psi(\mathbf{r};\mathbf{R})$ is the wavefunction of electronic ($\mathbf{r}$) and nuclear ($\mathbf{R}$) coordinates within the Born–Oppenheimer (BO) approximation. However, there is only one molecular system, namely H_2^+, for which the Schrödinger equation can be solved exactly. The difficulty in solving 2.1 arises from the complexity of the electron–electron potential energy in a many electron system. This problem can be overcome by the Hartree–Fock (HF) approach, in which the electron–electron potential energy is described by the motion of one electron in the average electric field due to all the other electrons and nucleus. This is done by introducing the Fock operator, which accounts for the electron motion in the average electric field. The total wavefunction in the HF approach is the product of one-electron wavefunctions (spin orbitals), in which the antisymmetry require-

ment is fulfilled by constructing the wavefunction from Slater determinants. An iterative solution of the Schrödinger equation within the HF approach can be obtained by the self-consistent-field (SCF) method. In this procedure trial spin orbitals are used to formulate the Fock operator. The HF equations are solved and a new set of spin orbitals are generated, and they are then used to formulate new Fock operator equations. This is repeated until a satifactory convergence is obtained. Since the HF approach neglects instantaneous electron–electron interactions, it neglects quantum mechanical effects on the electron distribution. In other words, the HF approach ignores electron correlations. Thus, in order to increase the accuacy of calculations, electron correlation methods need to be utilized. Such methods include configuration interaction (CI), the Møller–Plesset perturbation theory (MP), and coupled cluster (CC). The HF wavefuntions are used as a starting point for post-HF electron calculations including electron correlation.

In the CI theory, a single HF Slater determinant can be used to generate singly (S), doubly (D), triply (T)... excited determinants, and the trial wavefunction is written as a linear combination of ground and excited determinants

$$\Psi_{\mathrm{CI}} = a_0\phi_{\mathrm{HF}} + \sum_{\mathrm{S}} a_{\mathrm{S}}\phi_{\mathrm{S}} + \sum_{\mathrm{D}} a_{\mathrm{D}}\phi_{\mathrm{D}} + \sum_{\mathrm{T}} a_{\mathrm{T}}\phi_{\mathrm{T}} + \cdots = \sum_{i} a_i\phi_i, \qquad (2.2)$$

where a_i is the cofficient for determinant ϕ_i, and $\sum_i a_i\phi_i$ sums over all excited determinants i, ($i = 0$ corresponds to the ground state). The cofficients a_i are found by minimizing the energy. Computational resources and the size of the system set limits to the applicability of the CI theory, and the sum in equation 2.2 has to be truncated. At the CIS level of theory, only the singly excited determinats are included, and at the CISD level both singly and doubly excited determinant are included. The CI method can be used to describe the properties of excited states. Since the first (lowest) eigenvalue of the Schrödinger equation represents the ground state of the system, the second eigenvalue corresponds to the first excited state. The simplest approach is CIS, where only singly excited determinants are employed. The CIS method is used in Paper III to estimate electronic excitation energies of molecular complexes. Alternatively, equation-of-motion coupled cluster (EOM-CC) [52] or time-dependent density funtional theory (TD-DFT) [53] were used to estimate vertical excitation energies. More accurate methods were used to calculate excited states in Paper I, in which multi-configuration self-consistent field (MCSCF) calculations were used to describe the ground and excited state orbitals, and multi-reference configuration interaction (MRCI) calculations with the MCSCF orbitals were used to describe the ground and excited states of a system.

When the size of the system increases, more computational resources are needed. One of the common electron correlation methods is based on the Møller–Plesset perturbation theory. The Schrödinger equation can be written in the frame of the many-body perturbation theory as

$$\left(\widehat{H}_0 + \lambda \widehat{H}'\right) \Psi = E\Psi, \tag{2.3}$$

where $\widehat{H}_0$ and $\widehat{H}'$ are the unperturbed Hamilton operator and a small perturbation, respectively, and λ is a parameter determining the strength of the perturbation. In the MP theory $\widehat{H}_0$ is treated as a sum over one-electron Fock operators. Wavefuntions and energies can be expanded as Taylor expansions in the powers of the parameter λ. The truncation of the Taylor series determines the level of the MP theory. The first order MP theory gives the HF energy, and the electron correlation starts at second order. The acronym for the Møller–Plesset perturbation theory is MPn, where n = 2,3,... defines the order of the perturbation. Since the accuracy of electron correlation is quite satisfactory and its computational requirements are often lower than in the corresponding CI and CC methods, MP2 is commonly used to calculate structures and vibrational properties of larger systems [54]. The MP2 theory in utilized in Paper IV in order to find structures and vibrational properties of molecular complexes.

Basis sets are used to construct molecular orbitals from well-behaving functions. According to the molecular orbital theory, a linear combination of atomic orbitals is used to describe a molecular orbital. Gaussian type orbitals are commonly used in electronic structure calculations due to their computational efficiency. A split-valence 6–311++G** basis set was used in Paper III and Paper IV for hydrogen, carbon, oxygen, and fluorine [55–57]. In Paper I, an augmented correlation consistent polarized valence double zeta (aug-cc-pVDZ) basis set was used for hydrogen [58], while halogens and xenon were treated with an effective core potential (ECP), and only valence electrons were described explicitly [59–61].

Chapter 3

Results and discussion

3.1 Novel rare gas compounds

3.1.1 Electronic absorption spectra

The photodissociation of hydrogen halides, HCl, HBr, and HI, as well as HCN, H_2S, H_2O and H_2CO, in a xenon matrix and, especially, the electronic absorption spectra of the thermally induced products, are studied in Papers I and II.

The preparation of novel rare gas compounds is described in Chapter 1.3. Briefly, it can be simplified as a reaction between the thermally mobilized hydrogen atoms and XeY (Y = *e.g.* a halogen atom) pair. Hydrogen and halogen atoms can be easily produced in rare gas matrices by photolyzing hydrogen halides at photon energies sufficient for photodissociation and subsequent cage exit. Figure 3.1 shows the UV-absorption spectra of UV irradiated hydrogen halide-doped xenon matrices. After photolysis, the absorptions of halogen xenon charge-transfer [10] and the caged hydrogen atom [62, 63] were observed due to the photodissociation of the hydrogen halide molecule. After extensive photolysis, the temperature was increased to 45–50 K, at which diffusion of H atoms take place in solid xenon [35–39]. Upon annealing the absorption of caged hydrogen atoms disappeared and the intensity of the halogen–xenon charge transfer absorption was reduced by ca. 30 % due to the reaction of the thermally mobilized hydrogen atoms with the XeY pairs to form HXeY molecules (Fig. 3.1). The broad and structureless UV absorptions of HXeCl, HXeBr, and HXeI were assigned according to their correlation with the known IR absorptions [23].

Interestingly, the regeneration of HY via reaction H + Y $\rightarrow$ HY was observed to be a minor loss channel for hydrogen atoms. This means that ca. 70 % of the initially formed hydrogen atoms disappeared via different routes.

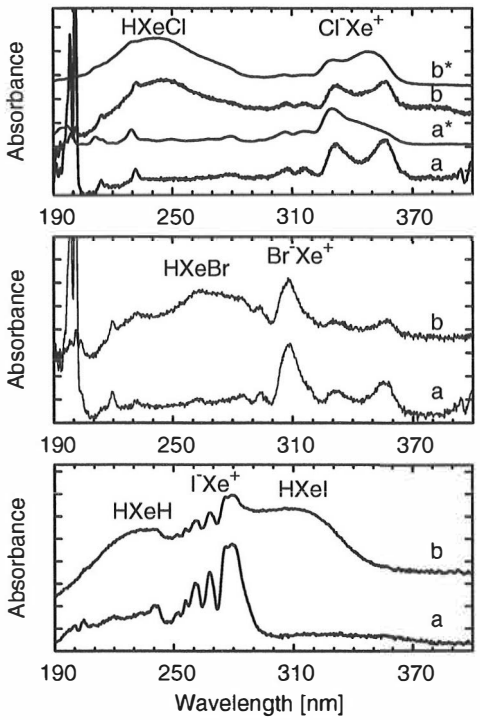

Figure 3.1: Electronic absorption spectra of HCl/Xe (top), HBr/Xe (middle), and HI/Xe (bottom) matrices: (a) after UV photodissociation of precursor, (b) after annealing at 45-50 K. Spectra measured from a free standing xenon crystal are marked with an asterisk. The weak absorption of the caged hydrogen in HI/Xe spectrum is most likely due to the low transmittance of the scattering matrix, not due to lower hydrogen concentration.

The formation of HXeH has been observed to be a significant trapping mechanism for hydrogen atoms [64]. These numbers are approximately consistent with the observation that ca. 40 % of the hydrogen atoms form HXeI [65]. However, the efficient UV photodissociation of HXeY molecules yielded only a partial recovery of hydrogen atoms, but full recovery of halogen atoms. This clearly indicates that some hydrogen atoms are lost in the annealing cycle. One suggested loss mechanism for hydrogen atoms is the formation of H_2 via the reaction $H + HXeY \rightarrow H_2 + Xe + Y$ [66].

The spectral widths and the absence of vibrational structure of the electronic absorptions of HXeY molecules indicate that these transitions are

from a bound ground state to a repulsive electronic excited state. Since the ground state possesses a strongly ionic character and photodecomposition of HXeY leads to the formation of a neutral species [65], these transitions involve a charge transfer process, where Y acts as a charge donor. This is consistent with the MRCI calculations on HXeCl, which predict that the electronic transition to the first excited state is a relatively pure intermolecular charge transfer transition from Cl to H whereas for less electronegative atoms Br and I, the charge tranfer c aracter of the transition is weaker. Very large transition dipole moments exceeding 7.0 D were estimated for HXeCl, HXeBr, and HXeI in Paper I.

The photodissociation of H_2O/Xe, H_2S/Xe, and H_2CO/Xe samples and, especially, the electronic absorption spectra of the thermally induced absorptions were studied in Paper II and in Ref. [67] (Fig. 3.2). In all samples very prominent absorption of the caged hydrogen was observed upon UV irradiation of the sample [62, 63]. In a HCN doped xenon matrix, the CN radical and the CN/Xe charge transfer absorptions were also observed [68]. In H_2O- and H_2S-doped xenon matrices, the absorptions of OH and SH radicals, as well as XeO and XeS charge transfer, were observed, and the spectral assignment were supported by the literature data [69–72]. The broad electronic absorptions of HXeY (Y = H, CN, SH, OH) appeared upon annealing the sample. An H_2CO-doped xenon sample was used to indentify the absorption of HXeH, which overlaps with other absorptions in other samples. The advantage of the H_2CO precursor is that only the absorption of HXeH was observed upon annealing. Again, the spectral assignment of the broad structureless UV absorptions was based on the correlation with the IR spectra and the photodecomposition profiles of the HXeY molecules.

The electronic absorptions can be most likely ascribed to transitions from a bound ground state to repulsive excited states and they are thus responsible for the efficient photodecomposition of the HXeY molecules. The efficient recovery of the neutral fragment Y during the photodissociation of HXeY implies a charge transfer character in the transition. The peak positions of the observed electronic absorption spectra are collected in Table 3.1.

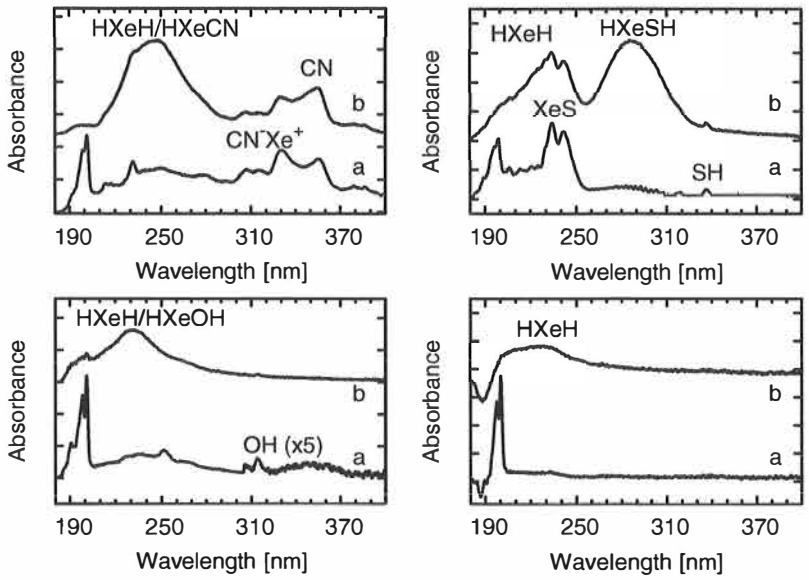

Figure 3.2: Electronic absorption spectra of HCN/Xe (top left), H_2S/Xe (top right), H_2O/Xe (bottom left), H_2CO/Xe (bottom right), matrices: (a) after UV photodissociation of precursor, (b) after annealing at 45-50 K. The negative peak in the H_2CO/Xe spectra is due to the bleaching of the precursor absorption upon photolysis.

Table 3.1: The wavelengths λ_{trs} of the electronic absorption spectra of HXeY.

	λ_{trs} [nm]	Reference
HXeH	230	Paper II
HXeCN	234[a]	Paper I
HXeOH	240	[67]
HXeCl	246	Paper I
HXeBr	262	Paper I
HXeSH	290	Paper II
HXeI	310	Paper I & Paper II
HXeI	410	Paper II

[a] Uncertain. Overlap with the HXeH absorption.

In Paper II the absorptions at 234 nm and 242 nm in the UV irradiated H_2S/Xe matrix were both assigned to the XeS charge transfer, but present analysis indicates that these absorptions in fact belong to different absorbers. Figure 3.3 shows the correlation between the integrated absorbances of the 242 nm absorption and the UV absorption of the SH radical. Based on this comparison, the absorption at 242 nm more likely belongs to the SH radical and it can be understood as a charge transfer absorption of the SH/Xe pair. This assignment is also supported by an empirical observation that charge transfer energy of Y/Xe (Y = halogen atom, CH, or SH) pair is linearly dependent on the electron affinity of Y (Fig. 3.4). SH and CN are pseudohalogens and hence similar energetics can be expected for them in solid xenon.

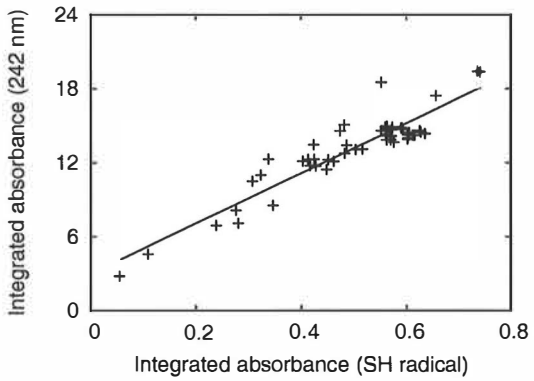

Figure 3.3: The correlation between UV absorbances of the 242 nm band and the SH radical absorption in irradiated H_2S/Xe matrix.

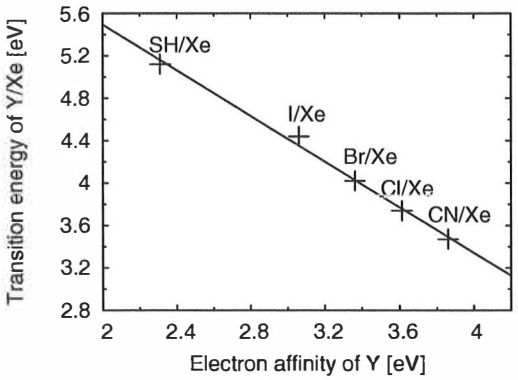

Figure 3.4: The transition energy of Y/Xe charge transfer plotted aginst the electron affinity of Y (Y = SH, I, Br, Cl, CN). Electron affinities of I, Br, and Cl are from Ref. [73] and for SH and CN from Refs. [74] and [75], respectively. Transition energies are from Paper I, Paper II, and Ref. [68].

3.1.2 On the formation and decomposition mechanisms

The formation of rare gas compounds is clearly related to the mobilization of hydrogen atoms in rare gas crystals. When matrices are annealed at temperatures above 40 K, a global, or in other words, long-range, migration of hydrogen atoms takes place. It has been observed that most of the hydrogen atoms disappear upon annealing and, simultaneuosly, rare gas molecules are formed [22, Paper I, Paper II]. This clearly indicates that the formation of rare gas molecules is related to the hydrogen atom trapping process. The partial recovery of hydrogen atoms upon photodissociation of HXeY molecules imply the excistence of some permanent loss channels for hydrogen atoms. A kinetic model has been developed to describe solid phase reactions due to thermally mobilized hydrogen atoms [66]:

$$\mathrm{H} + \mathrm{Xe} + \mathrm{H} \xrightarrow{k} \mathrm{HXeH} \tag{3.1}$$

$$\mathrm{H} + \mathrm{Xe} + \mathrm{Y} \xrightarrow{k} \mathrm{HXeY} \tag{3.2}$$

$$\mathrm{H} + \mathrm{HXeH} \xrightarrow{k} \mathrm{H_2} + \mathrm{Xe} + \mathrm{H} \tag{3.3}$$

$$\mathrm{H} + \mathrm{HXeY} \xrightarrow{k_1} \mathrm{H_2} + \mathrm{Xe} + \mathrm{Y} \tag{3.4}$$

$$\mathrm{H} + \mathrm{HXeY} \xrightarrow{k_2} \mathrm{H} + \mathrm{Xe} + \mathrm{HY} \tag{3.5}$$

These Reactions are considered to be controlled by hydrogen atom diffusion. Since the reaction radius d is assumed to be the same for all reactions, k

represents the rate constant ($k = k_1 + k_2$). The rate constant for the diffusion-controlled reaction 3.1 can be written in the form

$$k = 4\pi N_A D_{\mathrm{H}} d, \tag{3.6}$$

where N_A is the Avogadro number and D_{H} is the diffusion coefficient of the hydrogen atom [76]. The same rate constant can be used for all reactions, because only the hydrogen atom is diffusing and the other reactants are stationary. This is true as long as the reaction radius d is assumed to be the same for all reactions. The rate laws for the reactants involved in reactions 3.1–3.5 can be written as

$$\frac{\mathrm{d[H]}}{\mathrm{d}t} = -2k[\mathrm{H}]^2 - k[\mathrm{H}][\mathrm{Y}] - k_1[\mathrm{H}][\mathrm{HXeY}] \tag{3.7}$$

$$\frac{\mathrm{d[Y]}}{\mathrm{d}t} = -k[\mathrm{H}][\mathrm{Y}] + k_1[\mathrm{H}][\mathrm{HXeY}] \tag{3.8}$$

$$\frac{\mathrm{d[HXeH]}}{\mathrm{d}t} = k[\mathrm{H}]^2 - k[\mathrm{H}][\mathrm{HXeH}] \tag{3.9}$$

$$\frac{\mathrm{d[HXeY]}}{\mathrm{d}t} = k[\mathrm{H}][\mathrm{Y}] - \underbrace{(k_1 + k_2)}_{k}[\mathrm{H}][\mathrm{HXeY}] \tag{3.10}$$

$$\frac{\mathrm{d[H_2]}}{\mathrm{d}t} = k[\mathrm{H}][\mathrm{HXeH}] + k_1[\mathrm{H}][\mathrm{HXeY}] \tag{3.11}$$

$$\frac{\mathrm{d[HY]}}{\mathrm{d}t} = k_2[\mathrm{H}][\mathrm{HXeY}] \tag{3.12}$$

This model can be used to estimate the relative number of trapped hydrogen atoms in different trapping sites such as HXeY, HXeH, H_2, and HY. A general agreement between the experimental and computed values has been found in the case of HI doped xenon [66]. However, in Ref. [66] the experimental data for hydrogen atoms were not provided in the comparison. The following data are obtained from H_2S doped xenon and the results are compared with the predictions of the kinetic model.

Annealing of an irradiated H_2S-doped xenon matrix caused the formation of HXeH and HXeSH molecules and only a minor recovery of H_2S. Upon annealing, one third of the SH radicals were lost in reactions, while all hydrogen atoms disappeared. A subsequent photodecomposition of the rare gas molecules yielded a ca. 80 % recovery of hydrogen atoms; nearly full recovery of SH was observed. Moreover, a second annealing–irradiation cycle yielded a still higher relative recovery of hydrogen atoms. The recovery of hydrogen atoms in consecutive annealing-photodecompostition cycles is shown in Figure 3.5. While ca. 0.5 % of the initial amount of hydrogen atoms is lost after annealing at 42 K, HXeH has already reached its final absorbance and the

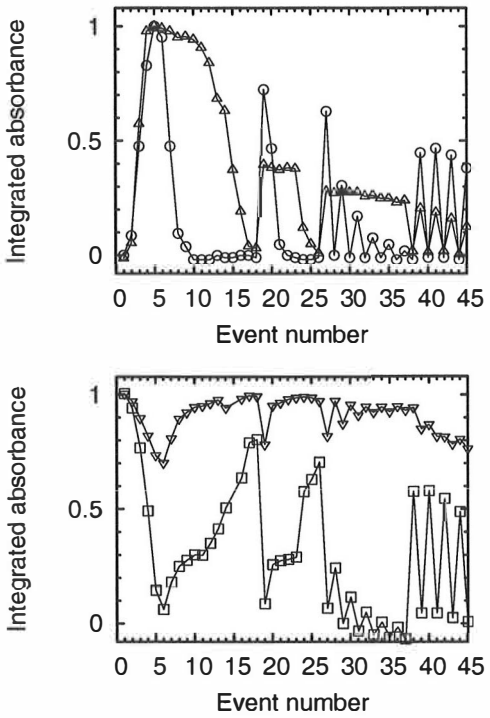

Figure 3.5: Integrated absorbances (in relative units) of the caged hydrogen (—□—), the SH radical (—▽—), HXeH (—△—), and HXeSH (—○—). Numbers on x-axis: 1: after UV irradiation of H_2/Xe (1:1000) matrix; 2–6: annealing at 35 K, 40 K, 42 K, 44 K, and 48 K; 7–10, 20–23, 28, 30, 32, 34, and 36 irradiation at 308 nm; 14–18, 24–26, 38, 40, 42, and 44 irradiation at 193 nm; 11–13 a broad band deuterium lamp irradiation; 19, 27, 29, 31, 33, 35, 37, 39, 41, 43, and 45 annealing at 48 K

HXeSH absorbance is ca. 80 % of its final value. Since the reactions between hydrogen atoms and HXeH have been proposed to set a limit to the amount of HXeH, the result means that the decomposition rate of HXeH has reached its formation rate. This agrees remarkably well with the kinetic model of the Helsinki group [66]. Finally, all hydrogen atoms disappeared while ca. 30 % of the initial SH radical content was consumed. A subsequent irradiation at 308 nm bleaches the HXeSH absorption, but it leaves the HXeH absorption unchanged and recovers 30 % of hydrogen atoms and nearly all the SH radicals. This is in agreement with the kinetic model, although the hydrogen

recovery is higher than proposed by the kinetic model [66]. The higher recovery of hydrogen is probably due to an initally higher relative hydrogen concentration, because dissociation of the SH radical increases the hydrogen atom concentration and decreases the SH radical concentration. The rapid evolution of hydrogen atoms at the early state of photolysis indicates that some amount of hydrogen atoms are formed in the photodissociation of the H_2S dimer. An irradiation at 193 nm bleaches the HXeH absorption and recovers 50 % more hydrogen. The total recovery of hydrogen atoms is 80 % after the first annealing photodecomposition cycle. Second annealing photodecomposition recovers nearly all hydrogen atoms and the SH radicals, but the relative amounts of HXeH and HXeSH are changed significantly. The first two annealing-photodecomposition cycles show that the recovery of hydrogen atoms from HXeH is about 60 % higher than the recovery from HXeSH. This is consistent with the results of Ref. [66].

The rate laws were solved numerically and the results obtained are compared with the experimental observations (see Figure 3.6). The initial concentrations were taken from an experimental estimate, which was $[H] = 4.5 \times [SH]$. Then branching the ratio between reactions 3.3 and 3.4 was set to $1 : 1$ ($k_1 : k_2 = 1, k_1 + k_2 = k$). Although the kinetic model is able to reproduce the experimentally observed relative amounts of HXeH and HXeSH, it fails to model correctly the hydrogen atoms and the SH radicals. The k_1 and k_2 values used are most probably too large, and thus the formation of H_2 and H_2S is overestimated. Almost 90 % of the intial hydrogen atom content is stored in H_2 molecules at the end of the kinetic modelling in Figure 3.6, while experimentally there is a substantial hydrogen atom concentration still left. The experimental data suggest smaller yields for HY and H_2, and thus a higher recovery of Y and H is obtained. The full recovery of the SH radical means that Reaction 3.5 is a minor reaction channel. Small losses of the SH radicals during annealing suggest a small probability for Reaction 3.2 or a high probability for Reaction 3.5. Since the reactions are diffusion controlled, the rate constants of Reactions 3.1 and 3.2 are assumed to be identical, so that the decomposition of HXeSH via Reaction 3.4 can be expected to be responsible for the small decrease of the SH radicals. The higher experimental recovery of the hydrogen atoms and SH radicals may indicate that other reaction channels could also exist. The reaction $H + S \rightarrow SH$ could be one possible explanation for the small decrease of SH, but the insignificant changes in the S atom concentration during the experiments do not support this possibility.

The complexity of the present experimental data does not provide a simple and confident test field for the kinetic model. Similar experiments in HI doped xenon matrix would afford a better and simpler test. However,

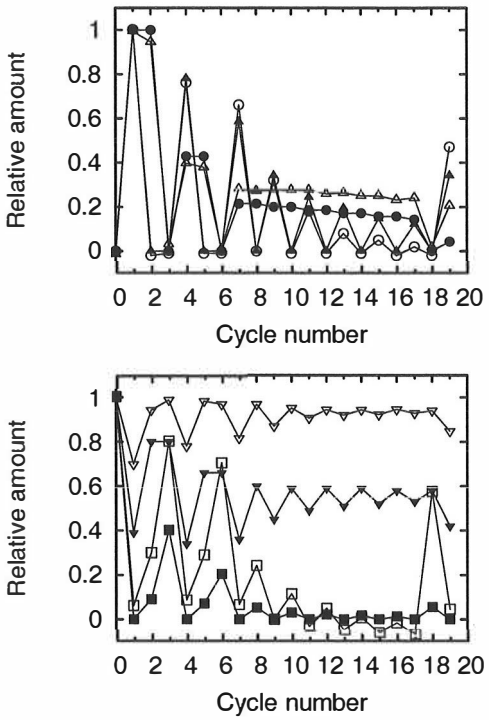

Figure 3.6: Relative amounts of caged hydrogen (experimental —□—; kinetic model —■—), SH radical (—▽—; —▼—), HXeH (—△—; —▲—), and HXeSH (—○—; —●—)

the present tests give more or less quantitative results about the reactivity of hydrogen atoms in solid xenon.

3.1.3 Comment on the usability of the UV absorption technique

Since the rare gas molecules have extremely intense IR absorptions of the H–Rg stretching vibration, IR spectroscopy has become a very powerful tool in the indentification of rare gas molecules [22]. However, in many cases the lack of information about atoms in IR spectroscopy leaves some open questions. One intresting question is the initial amount of hydrogen atoms and their recovery in the formation–decomposition cycles described earlier in this thesis. EPR is a very sensitive method for following the relative amounts of

hydrogen atoms, but it is limited to open shell species only. Moreover, combining EPR and IR is not a straightforward task. Typically, separate samples are needed for EPR and IR spectroscopy, and then very careful preparation of samples becomes essential. To obtain two identical matrices may be exhausting, since matrix morphology and matrix ratio are the most important parameters. Laser induced fluorecence (LIF) is a sensitive method for the detection of atoms, but its use has some limitations as well. LIF methods may destroy some information of the sample; for example, the LIF detection of hydrogen atoms in solid xenon efficiently destroys rare gas molecules. The detection of atoms in a rare gas matrix by UV absorption spectroscopy is a gentle method. The photon flux of an UV light source needed for UV absorption spectroscopy is relatively low and thus rare gas molecules are not significantly dissociated in the time scale of the detection. Of course, more work is needed to extract data from complex UV spectra as can be seen in Figure 3.7. From an experimentalist's point of view, UV (VUV–VIS) and IR absorption tehniques can be easily combained and the data can be collected from the same sample.

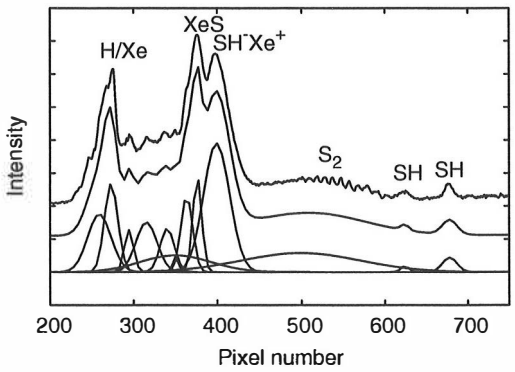

Figure 3.7: Fit of 13 gaussian functions to the experimental UV spectrum of UV irradiated H_2/Xe matrix. Upper trace: experimental spectrum, middle trace: fitted spectrum (sum of 13 gaussian functions), and lower traces: individual gaussian functions used in the fitting procedure.

3.1.4 Does HXeSH$\cdots$H$_2$S exist?

The capability of rare gas molecules to form complexes with neutral molecules has been confirmed both theoretically and experimentally. The vibrational

properties of rare gas compounds are very sensitive to intermolecular interactions and, hence, large blue-shifts of the H–Ar, H–Kr, H–Xe stretching vibrational modes are experimentally observed for the $HArF\cdots N_2$, $HKrF\cdots N_2$, $HKrCl\cdots N_2$, and $HXeOH\cdots H_2O$ complexes [77 79]. The stability and blue-shift of the H–Rg stretching mode of $HXeH\cdots H_2$ and $HArF\cdots CO$ complexes are theoretically predicted, while a large red-shift of the H–Ar stretching mode of $HArF\cdots P_2$ is predicted [80–82].

The $HXeOH\cdots H_2O$ complex provides the most relevant comparison with the present discussion, because the proposed $HXeSH\cdots H_2S$ would be its sulfur analog and somewhat similar properties could be expected [79]. The indirect observation that supports the formation of the proposed complex is the decrease of the IR absorbance of the $SH\cdots H_2S$ complex at 2550.3 cm^{-1} [83], when a UV-irradiated H_2S/Xe matrix is annealed at 48 K. One could expect a recovery of the H_2S dimer, when thermally mobilized hydrogen atom undergo a reaction with $SH\cdots H_2S$. However, the IR absorption of H_2S dimer remains unchanged, while the absorption of $SH\cdots H_2S$ decreases by 40 %. Figure 3.8(a) shows the decrease of the $SH\cdots H_2S$ absorption at 2550.3 cm^{-1} upon annealing, and its 90 % recovery during subsequent irradiation at 308 nm. The IR absorptions of the thermal products and their photostability are shown in Figure 3.8(b). The appearance of the IR absorptions of HXeH and HXeSH are indicators for reactions between thermally mobilized hydrogen atoms and XeH and XeSH pairs, respectively [25, 27]. In addition to the known bands, weaker absorptions appeared on the blue side of the HXeSH absorptions. Irradiation at 308 nm bleached these thermally induced absorptions as well as the absorptions of HXeSH, while the absorptions of HXeH were unchanged. In addition, the irradiation recovered the $SH\cdots H_2S$ absorption.

The thermally induced absorptions at 1326 cm^{-1}, 1231 cm^{-1}, and around 1192 cm^{-1} are blue shifted by ca. 207 cm^{-1}, 112 cm^{-1}, and 73 cm^{-1}, respectively, withrespect to the H–Xe stretching fundamental of HXeSH. If these shifts are compared with the blue shift of ca. 103 cm^{-1} and 164 cm^{-1} of $HXeOH\cdots H_2O$ and $HXeOH\cdots (H_2O)_2$, respectively, it can be concluded that the observed peaks are not too much blue-shifted to belong to the $HXeSH\cdots H_2S$ complex.

A computational analysis of the vibrational spectrum of the complex was carried out during this study. The initial structure of the $HXeSH\cdots H_2S$ complex was built from the structural parameters of the HXeSH molecule [25] and the $HXeOH\cdots H_2O$ complex [79], its and geometry and harmonic frequencies were computed at the MP2 level of theory with the aug-cc-pVDZ basis set for H [58] and S [84]; for Xe The Stuttgart RLC ECP [59] was used [57]. The results obtained are collected in Table 3.2 and the structure of the

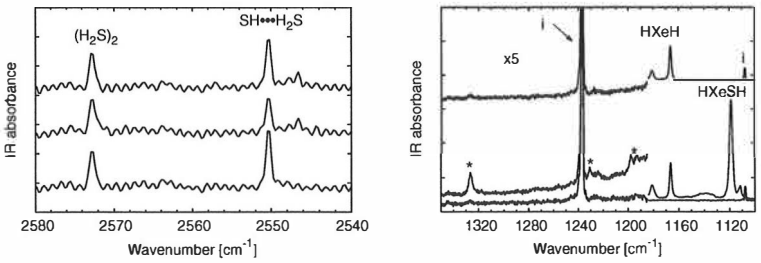

(a) $(H_2S)_2$ dimer and $SH\cdots H_2S$ complex

(b) Thermal products

Figure 3.8: The IR spectrum of a H_2S/Xe matrix (1:1000, T_d = 48 K). Lower spectra: after UV irradiation, middle spectra: annealing at 48 K, upper spectra: irradiation at 308 nm. i indicates impurity peaks that are stable against irradiation and annealing. The thermally induced absorptions are marked with an asterisk.

$HXeSH\cdots H_2S$ complex is shown in Figure 3.9.

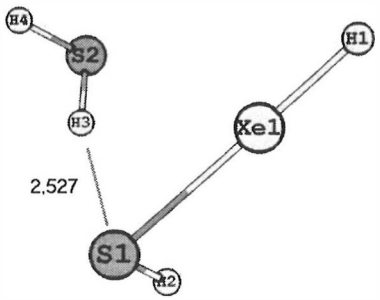

Figure 3.9: Optimized structure of the $HXeSH\cdots H_2S$ complex.

Computationally the H–Xe vibrational frequency of HXeSH is blue shifted by ca. 65 cm^{-1} upon complexation. This is roughly half of the blue shift obtained for the HXeOH–water complex [79]. The comparison of hydrogen bond lengths in both complexes shows that the $-O\cdots HOH-$ hydrogen bond is nearly 1 Å shorter than the corresponding $-S\cdots HSH-$ hydrogen bond. The proposed weaker hydrogen bonding in the $HXeSH\cdots H_2S$ complex causes smaller effects on the remote part of HXeSH, and consequently smaller shifts in the H–Xe vibrational frequency. Although the S–H vibra-

Table 3.2: The calculated structural parameters and harmonic vibrational frequencies of HXeSH and HXeSH$\cdots$H$_2$S. The Bond distances are given in Å and the bond angles in degrees. The predicted IR intensities are given in parenthesis.

	HXeSH			HXeSH$\cdots$H$_2$S
	MP2	MP2 Ref. [25]	Expt. Ref. [25]	
	Structure			
r(H1–Xe1)	1.776	1.774		1.754
r(S1 Xe1)	2.731	2.729		2.752
r(H2–S1)	1.345	1.334		1.355
a(H2–S1–Xe1)	91.4	91.0		91.9
a(S1–Xe1–H1)	179.3	180.0		179.2
r(H3–S1)				2.527
r(H3–S2)				1.363
r(H4 S2)				1.350
a(H3–S2–H4)				92.7
	Frequencies (in cm^{-1})			
H3–S2–H4 asym. str.				2764.9 (2)
S1 H2 str.	2722.1 (7)	2729.9 (8)		2719.6 (5)
H3–S2–H3 asym. str.				2588.9 (291)
Xe1–H1 str.	1476.9 (2718)	1520.6 (3149)	1118.6	1542.3 (2485)
H3–S2–H4 bend				1201.1 (6)
asym. bend[a]	631.2 (2)	652.6 (2)		623.5 (3)
H1–Xe1–S1 bend	526.7 (0.02)	546.6 (4)		525.8 (0.4)
sym. bend[b]	450.0 (3)	472.5 (11)		440.5 (2)
H3 OPLA[c]				406.9 (35)
Xe1–S1 stretch	254.3 (45)	251.4 (37)		248.2 (50)

a H1–(Xe1–S1)–H2 antisymmetric bend
b H1–(Xe1–S1)–H2 symmetric bend
c Out of H4–S2 Xe1 plane vibration of H3

tional frequency in the –HS–H$\cdots$S– hydrogen bond is red-shifted only by few wavenumbers, the Xe–H frequency possesses a significant blue shift. The sensitivity of the H–Xe vibrational frequency to the complex formation can be understood by the charge transfer nature of the HXeY compounds [22].

The experimentally observed IR absorptions on the blue side of the HXeSH absorptions are in agreement with computational data. However, these absorptions can not be unambiguously assigned to the HXeSH$\cdots$H$_2$S complexes, although their behaviour upon annealing and irradiation is very similar to that the HXeSH molecule. The formation and the decomposition of unknown bands are related to the decrease and increase, respectively, of

the $SH\cdots H_2S$ absorption intensity, as well. The most intensive unknown thermally induced IR absorption was ca. 207 cm^{-1} blue-shifted with respect to the HXeSH. This is far too much for it to belong to the complex. In the case of $HXeOH\cdots(H_2O)_n$ the blue shift of the H–Xe vibrational frequency increased with increasing n, while the IR intensity of the H Xe vibration decreased [79]. It is not very obvious that the 207 cm^{-1} blue shifted band belongs to complexes with $n > 1$, since the experiments were carried out in relatively monomeric matrices. The absorptions that are blue-shifted by ca. 112 cm^{-1} and 73 cm^{-1} are closer to the computational values, and these absorption can be tentatively regarded as candidates for the IR absorptions of $HXeSH\cdots H_2S$ complexes. However, a more systematic study of these absorptions should be carried out to provide a clear-cut assignment.

3.2 Formyl fluoride

3.2.1 Infrared spectrum of HCOF and HCOF dimer

The infrared spectra of HCOF and HCOF dimer in Ar, Kr, and Xe matrices are shown in Figure 3.10. In a dilute sample (HCOF/Rg = 1:2000) five out of six vibrational modes of monomer and two dimer bands were reliably observed. It was found that all monomer vibrational bands are split into two lines due to matrix site effects [3]. In Kr and Xe matrices the corresponding monomer and dimer absorptions are shifted from the argon matrix values. The IR absorptions of HCOF and its dimers in Kr and Xe matrices were assigned according to the Ar matrix data [85, Paper III, Paper IV].

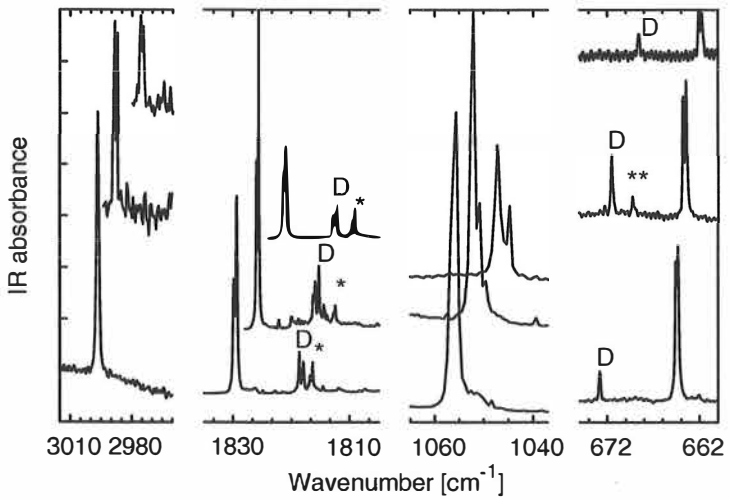

Figure 3.10: IR absorptions of HCOF and HCOF dimer in rare gas matrices. Lowest spectra: in Ar (T_d = 15 K, annealed at 35 K), middle spectra: in Kr (T_d = 20 K, annealed at 40 K), uppermost spectra: in Xe (T_d = 35 K, annealed at 50 K). D indicates dimer absorptions and (*) and (**) indicate impurity-induced absorption and gas-phase CO_2 absorption, respectively. Note: the absorbances of different bands are scaled. The shown spectral regions from the left to right correspond to C–H stretching, C–O stretching, C–F streching, and FCO bending regions of HCOF.

Another feature of the HCOF monomer absorptions was the appearance of broad red-shifted shoulder bands. A broad red-shifted shoulder band of monomeric CO absorption was observed, too. Typically, minor amounts

of carbon monoxide were present in the samples due to the decomposition of HCOF on the walls of the deposition system [85, Paper III]. Despite the decomposition of HCOF, no absorption of hydrogen fluoride was observed in the IR spectrum [PaperIII, PaperIV]. Upon annealing the matrix, the red-shifted shoulder bands disappeared and the known dimer bands increased in intensity (Fig. 3.11). The intensity of the CO absorption decreased upon annealing, as well. These shoulder bands were absent in the samples deposited at higher temperatures. According to experimental observation these shoulder bands were assigned to some thermally unstable species, for example, two or more HCOF molecules located nearby in a non-equilibrium geometry, or HCOF interacting with another molecule. Experimental observations suggested non-equilibrium structures of HCOF dimers and HCOF$\cdots$CO complexes [Paper IV].

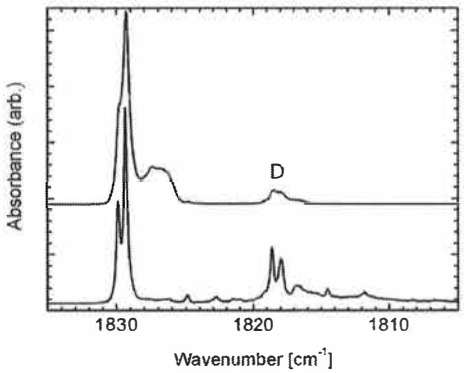

Figure 3.11: The IR absorption of the CO stretching mode of HCOF in argon matrix (HCOF/Ar = 1/500) Upper trace: after deposition at 10 K, lower trace: annealing at 30 K. D indicates dimer band.

In samples of higher concentration (HCOF/Rg = 1:500–1:250, Rg = Ar, Kr), a number of new lines appeared around the monomer and dimer absorptions and, interestingly, new absorptions became visible on the higher energy side of the C–H streching absorption of the monomer (Fig. 3.12) [Paper IV]. This absorption showed the same behavior as the known HCOF dimer absorptions when experimental parameters, such as deposition temperature and matrix ratio, were varied. Thus, the absorptions at 3013 cm^{-1} in Ar and 3007 cm^{-1} in Kr are tentatively assigned to the HCOF dimer. The spectral assignments of these bands were supported by the computational

studies of the HCOF dimer by Kovács et. al. [86], and by the author of this thesis in Paper IV.

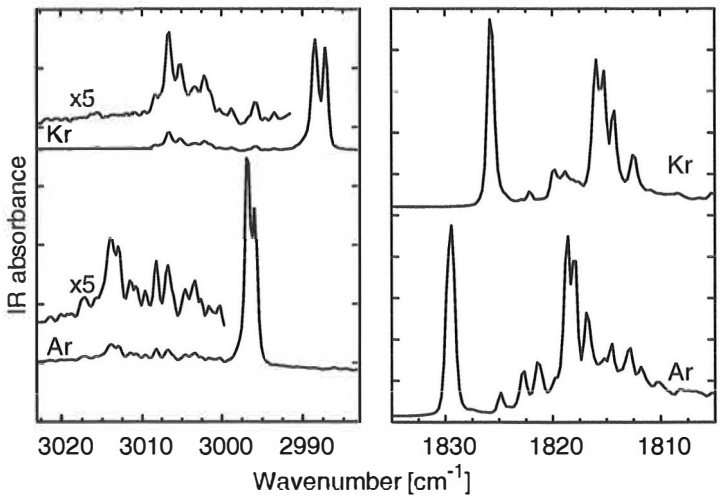

Figure 3.12: IR spectra of C–H and C–O stretching region of HCOF in Ar (1:500, T_d = 25 K) and in Kr (1:500, T_d = 30 K).

Experiments on CO-doped HCOF/Ar matrices were carried out in order to exclude the HCOF$\cdots$CO complex absorptions as the origin of the 3013 cm^{-1} absorption. New absorptions appeared on the left side of the C–H stretching mode when CO was added, while the 3013 cm^{-1} absorption disappered (Fig. 3.13). Additionally, the HCOF monomer and dimer absorption intensities were signifigantly reduced and new lines appeared close to the isolated CO absorption. This indicates that CO has a great tendency to form complexes with HCOF. These observations supported the assignment of the 3013 cm^{-1} absorption to the HCOF dimer.

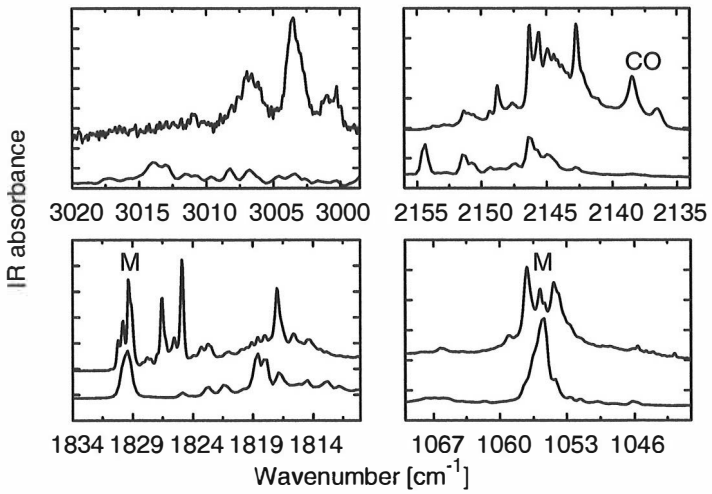

Figure 3.13: The IR spectrum of a CO-doped HCOF/Ar matrix. Upper trace: CO/HCOF/Ar = 1:1:500, T_d = 25 K. Lower trace: HCOF/Ar = 1:500, T_d = 25 K. M indicates the HCOF monomer.

3.2.2 Structure of the HCOF dimer

In order to describe the IR spectrum and the structure of the HCOF dimer, MP2/6-311++G** calculations with all electrons correlated were carried out for the six structures, that have been found stable [86]. The basis set superposition (BSSE) error for the dimerization energies was corrected according to the counterpoise (CP) method [87]:

$$\Delta^{\mathrm{CP}}_{\mathrm{AB}}E(R) = E_{\mathrm{AB}}(R) - E^{\mathrm{CP}}_{\mathrm{A}}(R) - E^{\mathrm{CP}}_{\mathrm{B}}(R), \tag{3.13}$$

where $\Delta^{\mathrm{CP}}_{\mathrm{AB}}E(R)$ is the BSSE correction for the interaction energy of two molecules A and B at distance R, $E_{\mathrm{AB}}(R)$ is the total (BSSE uncorrected) interaction energy, and $E^{\mathrm{CP}}_{\mathrm{A}}(R)$ represents the energy of the individual A molecule calculated by adding the basis set of molecule B at a distance R from molecule A. Similarly, $E^{\mathrm{CP}}_{\mathrm{B}}$ represents the energy of the molecule B, when A's basis set is included. The BSSE leads to an artifical lowering of the dimerization energy, and it needs to be corrected in order to find the correct structures. Typically, the error originating from the BSSE in weak hydrogen-bonded complexes at the MP2/6–311++G** level of theory is 30–50 % of the total interaction energy [88]. Often, the BSSE is corrected only for the final structure, while the optimization follows a BSSE-uncorrected

route. Including the BSSE correction in optimization of the geometry might lead to substantially different results from those of the BSSE-uncorrected procedure. This was demonstrated for the HCOF dimers in Paper IV. The BSSE correction by CP procedure is implemented in the geometry optimization procedure in the Gaussian03 software, which provides a straightforward method for the BSSE-corrected optimization [47].

The optimized structures of the HCOF dimers are shown in Figure 3.14. Four structures (I–IV in Fig. 3.14) were found stable when geometry optimization was carried out with the BSSE correction. Two structures (V and VI in Fig. 3.14) were stable only if the geometry optimization was carried out without the BSSE correction. This was a surprising result, be-

Table 3.3: Computed (MP2(FULL)/6-311++G**) dimerization energies (in kJ/mol). The BSSE-uncorrected energies (MP2/6-311++G**) are from Ref. [86]. Dimerization energies are corrected for zero-point energy from a harmonic frequency analysis.

	I	II	III	IV	V	VI
BSSE-corrected	-6.6	-9.6	-7.4	-5.0		
BSSE-uncorrected	-8.5	-13.2	-10.9	-8.4	-11.9	-9.7

cause structure V has the second lowest dimerization energy according to the BSSE-uncorrected calculations [86]. The comparison of the BSSE-corrected and -uncorrected energies in Table 3.3 shows that the corrected energies are substantially higher than the uncorrected ones. Thus the effect of the BSSE correction is to compensate for the reduction of the dimerization energy arising from the BSSE. The BSSE in the HCOF dimers was 20–40 % of the dimerization energy at the MP2/6-311++G** level of theory. However, it is observed that the MP2/6–311++G** level of theory underestimates the dispersion energy of formaldehyde (H_2CO) dimers and thus gives too low dimerization energies, which leads to an increse of the intermolecular bond lengths [86]. The BSSE correction futher decreases the dimerization energy of H_2CO dimers. The BSSE-corrected optimization of HCOF dimers caused elongation of –H$\cdots$O– and –H$\cdots$O– hydrogen bonds by ca. 0.07 Å and 0.1–0.13 Å, respectively, relative to the BSSE-uncorrected values [Paper IV]. The inability of the 6–311++G** basis set to describe dispersion energy, combined with the effect of the BSSE correction, lead to a substantially smaller dimerization energy than obtained with the augmented diffuse basis sets [86]. It has been suggested that the BSSE-uncorrected calculations on H_2CO and HCOF dimers give a better description of molecular properties than the BSSE-corrected ones at the MP2/6–311++G** level of theory.[86]

The calculations of dimer properties become more time demanding if large diffuse basis sets are used. In paper IV a compromise between the accuracy and computer time led us to select the MP2/6-311++G** level of theory. It is necessary to emhasize that the methodological differences of the BSSE corrections give somewhat different results, but these calculations are allways approximations of real systems and the methods used in Paper IV are believed to yield a satisfactory description of the system.

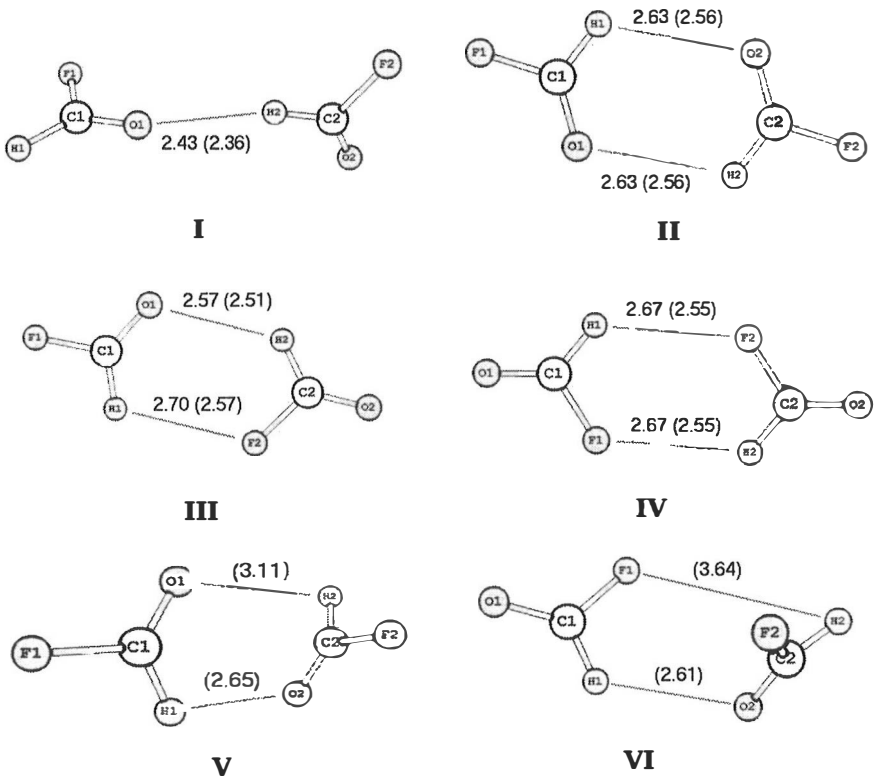

Figure 3.14: Optimized structures of the HCOF dimer obtained at the MP2(FULL)/6-311++G** level of theory. Hydrogen bond lengths are shown in Ångströms. Values in parenthesis are obtained without the BSSE correction.

The harmonic frequencies of HCOF and HCOF dimers were computed for the optimized structures I–IV (Fig. 3.14) in order to support the IR assignments of the blue-shifted C–H bands. The spectral shifts of the dimer

vibrations with respect to the HCOF monomer vibrations are shown in Table 3.4 and in Figure 3.15. It is obvious that the observed IR spectra are not likely to belong to structures I, III, and IV, because both red- and blue-shifted bands should be observed for the FCO bending and CF stretching modes of structures I, III, and IV. This leaves only one candidate for the observed dimer, which is structure II. The computed vibrational shifts of structure II match very well the observed IR shifts in Figure 3.15. Based on the good correlation between experimental and computational results, the most stable structure II is suggsted to be the most abundant dimer in the matrix.

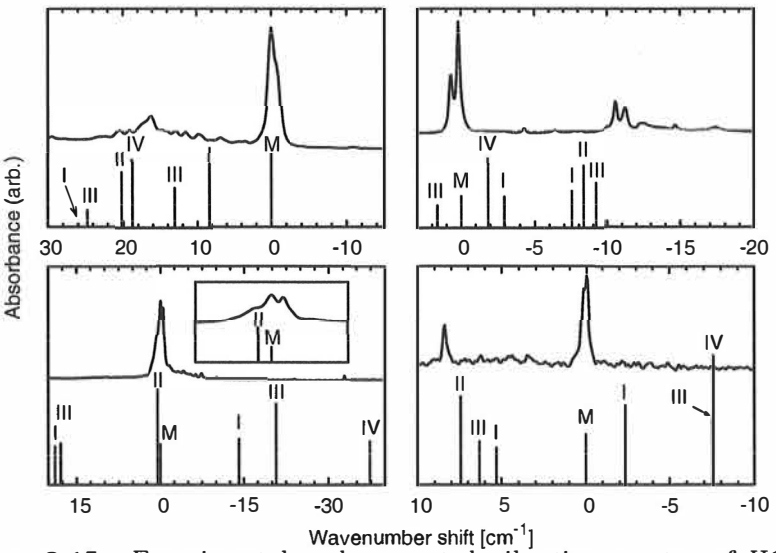

Figure 3.15: Experimental and computed vibration spectra of HCOF monomer (M) and HCOF dimers (structures I–IV). The values on the x-axes correspond to the relative shift from the monomer line. The computed spectra are shifted to match the experimental monomer lines.

Table 3.4: The spectral shifts $\tilde{\nu}_{\text{dimer}} - \tilde{\nu}_{\text{monomer}}$ (in cm^{-1}) of different vibrational modes.

		calcd.					
	expt.	I	II	II	IV	V[a]	VI[a]
$\tilde{\nu}$(OH)	16.3/17.1	8.4/26.0	20.3	13.1/24.7	18.8	10.0/21.8	14.3/23.5
$\tilde{\nu}$(CO)	-10.8 – -11.9	-3.0/-7.5	8.3	-9.2/1.6	-1.9	-10.4/-4.0	-6.1/-0.5
$\tilde{\nu}$(HCF)	vw[b]	1.6/12.5	0.2	2.0/-5.5	1.6	-1.0/5.5	-3.7/1.3
$\tilde{\nu}$(CF)	0.2/0.7	18.8/-14.1	0.5	17.8/-37.3	-20.7	5.1/16.5	-27.8/4.2
$\tilde{\nu}$(opla)[c]	vw[b]	4.6/14.0	15.5	11.2/9.3	2.1	-1.1/12.4	0.8/8.0
$\tilde{\nu}$(FCO)	7.7/7.9	5.3/-2.3	7.4	-7.5/6.3	7.5	3.5/7.6	-4.8/4.9

a BSSE-uncorrected data.
b Not reliably observed, very weak absorption.
c Out of plane vibration of hydrogen atom.

3.2.3 Photodissociation of formyl fluoride

The photodissociation of formyl fluoride following the electronic excitation from electronic $\tilde{\text{X}}\,(^1\text{A}'')$ ground state to electronic $\tilde{\text{A}}\,(^1\text{A}')$ exited state has been studied in the gas phase [89–96]. Based on the experimental observations photodissociation of HCOF follows the following pathways:

$$\text{HCOF}\,(\tilde{\text{X}}\,^1\text{A}'') \xrightarrow{h\nu} \text{HCOF}\,(\tilde{\text{A}}\,^1\text{A}') \rightarrow \text{HF}\,(\text{X}\,^1\Sigma^+) + \text{CO}\,(\text{X}\,^1\Sigma^+) \quad (3.14)$$

$$\rightarrow \text{H}\,(^2\text{S}) + \text{FCO}\,(\text{X}\,^2\text{A}') \quad (3.15)$$

$$\rightarrow \text{F}\,(^2\text{P}) + \text{HCO}\,(\text{X}\,^2\text{A}') \quad (3.16)$$

$$\rightarrow \text{H}\,(^2\text{S}) + \text{F}\,(^2\text{P}) + \text{CO}\,(\text{X}\,^1\Sigma^+) \quad (3.17)$$

Since the HCOF molecule is excited to the first electronic singlet state (S_1), the radiationless decay can proceed via channels 3.14–3.17. Internal conversion (IC) to the ground state (S_0) is involved in the molecular dissociation channel 3.14, and the dissociation on the S_0 surface proceeds via highly excited vibrational levels of HCOF [90]. An intersystem crossing (ISC) from S_0 to the T_1 surface, and subsequent passage over the energy barrier (or through it by tunneling) to the T_1 product asymptote, is assumed to be responsible for the C–F and C–H bond cleavage channels 3.15 and 3.16 [92]. However, theoretical analysis gives a very small rate coeffiecient for channel 3.16 relative to channel 3.15 on the T_1 surface; thus, an alternative mechanism is proposed for the C–F bond cleavage [97]. Theoretical RRKM calculations support the C–F bond cleavage on the S_1 surface at excitation wavelengths shorter than 233 nm, which is consistent with experimental results [93, 96]. Channel 3.17 is not studied in detail, although some experimetal evidence exists for its role [91].

Photodissociation studies of HCOF were carried out at 193 nm and 248 nm in Ar, Kr, and Xe matrices. In the Ar matrix, a number of product absorptions were observed in the C–O and H–F stretching regions of the CO$\cdots$HF and OC$\cdots$HF complexes upon photodissociation (Fig. 3.16). Upon annealing the photolysed sample, the absorptions of the CO$\cdots$HF and OC$\cdots$HF complexes increased significantly, while others decreased. Thus, the photodissociation products were mainly in-cage complexes between CO and HF in a more or less distorted geometry, hereafter referred as CO/HF as distinct from the more stable geometry. No photodissociation products due to C–F or C–H bond cleavage channels were observed in the argon matrix. This is interesting, because the gas phase branching ratio for channel 3.14 at 193 nm is 0.06, while it is 0.66 and 0.28 for the C–F and C–H bond cleavage channels, respectively [96].

Photodissociation at 193 nm provides 2.1 eV excess energy to be shared between the dissociation products of channel 3.15 [93]. If 233 nm (5.3 eV) is considered as the threshold wavelength for photodissociation via channel 3.16 on the S_1 surface, the photodissociation at 193 nm provides 1.1 eV excess energy. It is estimated that 49 % and 40–46 % of the total excess energy involved in the dissociation via channels 3.15 and 3.16, respectively, is released as translational energy [96]. As a light particle, a hydrogen atom absorbs nearly all of the excess translational energy. This yields 1 eV of kinetic energy for the hydrogen atom, which is well below the energy needed for cage exit in a solid matrix [7]. Obviously, the excess energy provided at 248 nm is not sufficient to promote cage exit either. The same argument can be used to explain the unsuccessful cage exit of the fluorine atom. Thus, the formation of the CO/HF complexes can be rationalized as the result of in-cage reactions of the dissociation products, *i.e.*, H + FCO $\rightarrow$ CO/HF, F + HCO $\rightarrow$ CO/HF, and HF + CO $\rightarrow$ CO/HF.

In Kr and Xe matrices, photodissociation products appeared in the C–O and H–F stretching regions of the CO$\cdots$HF and OC$\cdots$HF complexes, as in the argon matrix. However, the absorptions of these CO/HF complexes were subsequently photobleached at 193 nm and 248 nm. In Kr and Xe matrices traces of H, F, CO, CO_2, F_2CO, FCO, and HRg^+ (Rg = Kr or Xe) were also observed, which could imply the importance of other dissociation channels. However, the photodissociation of dimers, and, of course, the photodissociation of CO/HF complexes, can also be the origin of these photodissociation products. It should be noted that the CO/HF complexes were stable in photolysis in an Ar matrix, and isolated CO and HF were not dissociated in our experiments.

The progress of photodissociation of HCOF was followed by monitoring the integrated absorbance of the C–H stretching mode as a function of the

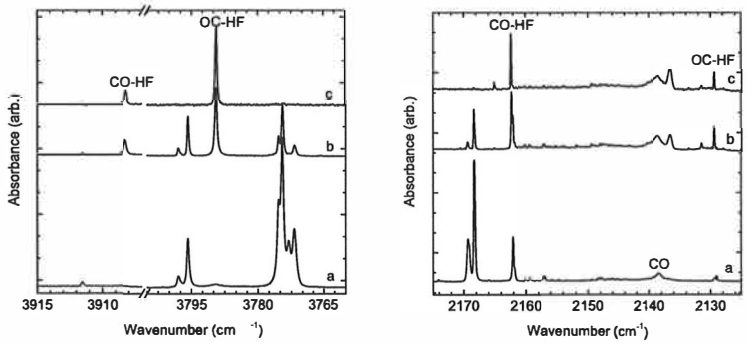

Figure 3.16: IR spectrum of the products formed in the photolysis of HCOF in an argon matrix: (a) after photolysis at 248 nm, (b) subsequent annealing at 35 K, and (c) at 40 K.

number of laser pulses deposited in the sample. Figure 3.17 shows decay curves of HCOF in the Ar, Kr, and Xe matrices. The rate of disappearance of HCOF follows first-order kinetics:

$$A = A_0 \mathrm{e}^{-kn}, \tag{3.18}$$

where A is the integrated absorbance, $A_0 = A(n = 0)$, n is the number of photons/cm^2 accumulated in the sample, and $k = \sum_i k_i$ represents the effective photodissociation cross-section (in cm^2) due to all possible dissociation channels i. The photodissociation cross sections obtained for HCOF at 193 nm and 248 nm are collected in Table 3.5. The higher photodissociation

Table 3.5: Photodissociation cross sections of HCOF (in 10^{-21} cm^2) at 193 nm and 248 nm. For details see equations 3.18 and 3.19 and Figures 3.17 and 3.19

	248 nm			193 nm		
	k	k_1	k_2	k	k_1	k_2
Ar	5.4	6.4		300	340	
Kr	13	12	1.3	240	210	3.5
Xe	67	85	2.2	360	110	15

efficiency of HCOF at 193 nm is explained by a larger gas-phase absorption cross section at 193 nm than at 248 nm [98]. An order of magnitude higher

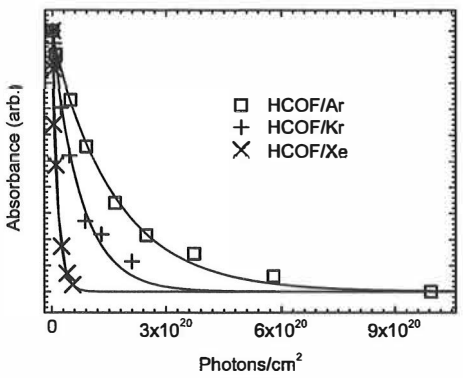

Figure 3.17: Decay of the IR absorbance of HCOF in Ar, Kr, and Xe matrices in 248 nm photolysis. Solid line represent fit of first-order kinetics.

UV absorbance of HCOF at 193 nm is observed in rare gas matrices, as well (Fig. 3.18). In heavier rare gases the photodissociation efficiency increases and it is ca. 10 times more efficent in Xe than in Ar.

The growth and decay of CO/HF complexes upon photodissociation of HCOF at 193 nm and 248 nm folllows first-order kinetics (Fig. 3.19):

$$\text{HCOF} \xrightarrow{k_1} \text{CO/HF complexes} \xrightarrow{k_2} \text{products}, \tag{3.19}$$

which leads to an integrated formula:

$$A_2 = A_2^{(0)} \mathrm{e}^{-k_2 n} + \frac{k_1 A_1^{(0)}}{k_2 - k_1} \left(\mathrm{e}^{-k_1 n} - \mathrm{e}^{-k_2 n} \right), \tag{3.20}$$

where A_2 is the integrated absorbance of the CO/HF complexes, $A_2^{(0)}$ and $A_1^{(0)}$ represent the initial integrated absorbances of the CO/HF complexes and HCOF, respectively. k_1 and k_2 are cross sections for the decay of HCOF and the CO/HF complexes, respectively. The obtained cross sections are collected in Table 3.5.

In Paper III, the photodissociation of the CO/HF complexes in Kr was reported as a single-photon process at 248 nm. Since photoinduced excitonic processess and harpoon reactions involve multiphoton excitation, these processes can be excluded [7]. Quantum chemical calculations were carried out to estimate the electronic vertical excitation energies of CO$\cdots$HF and

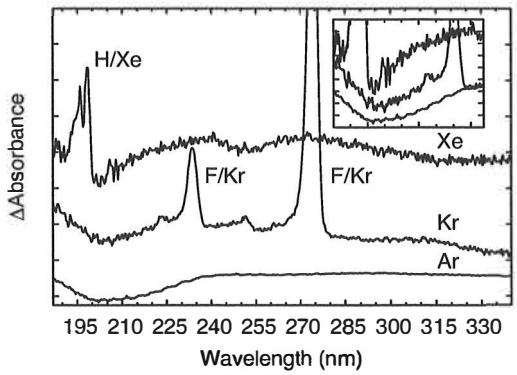

Figure 3.18: A difference UV absorption spectrum of HCOF/Ar after extensive 193 nm irradiation. The broad negative signal at ca. 200 nm is due to photobleaching of HCOF at 193 nm irradiation.

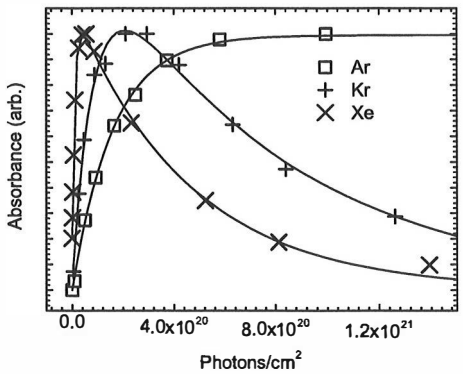

Figure 3.19: Growth and decay of CO/HF complexes upon photolysis of a HCOF/Rg sample at 248 nm. Experimental data are fitted to the formula of equation 3.20.

OC···HF complexes in their ground state equlibrium geometry [PaperIII]. These calculations showed that the electronic states of HF and CO are only slightly perturbed in complexes, and the first excited electronic states of the complexes are inaccessible to photon energies at 193 nm and 248 nm. This rules out dissociation processes due to electronic exitation to excited states within the intemolecular potential of the geminate guests [12]. It should be

noted that calculations were carried out only for CO···HF and OC···HF complexes and the effects of the solid environment were neglected.

In the present investigation, the effects of the zero-point vibration of the HF molecule are taken into account. The wavefunction of the lowest vibrational level was built up within the harmonic approximation, and experimental parameters are obtained from the literature [99]. In this approximation, the zero-point vibration of the H–F stretching is approximated by the zero-point vibration of the HF molecule, and the effects of the complex formation on the zero-point motion are neglected. Since the fluorine atom is heavier, the H–F stretching is approximated as a hydrogen atom movement relative to a stationary fluorine atom. Figure 3.20 shows the vertical excitation energies of the CO···HF complex when the H–F bond length is varied. In this model, only the hydrogen atom is moved, while the others are stationary. The vertical excitation energy of CO···HF is constant within the

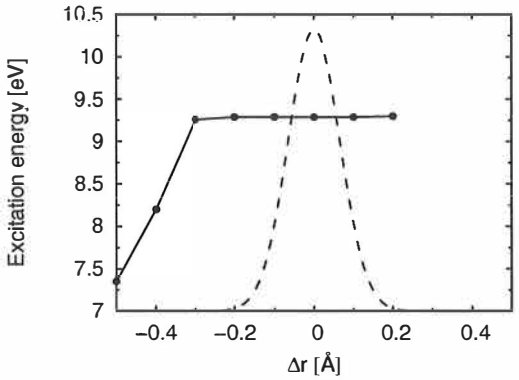

Figure 3.20: Computational (CIS/6-311++G**) vertical excitation energies of the CO-HF complex when the H–F bond length is varied. The dashed line represents the harmonic wavefunction of the lowest vibrational state of the H–F stretching. Δr represents changes in the intermolecular O–H bond length, while the H–F bond length is varied.

amplitude of the zero-point vibration of the hydrogen atom. The excitation energies decreased by ~1 eV, when the H–F bond was stretched by 0.4 Å from its equilibrium value. A further increase of the H–F bond length by 0.1 Å decreased the excitation energy by an additional 0.85 eV. However, an elongation of the H–F bond by 0.5 Å is too much to be caused by the zero-point motion of the hydrogen atom itself. Similarly, the amplitude of the zero-point vibration of the hydrogen atom is too small to cause signifincant changes in the excitation energy of the OC···HF complex.

The longest intramolecular distance between atoms in the HCOF molecule is 2.2 Å, and if the carbon atom is placed at the origin, the molecule can fit in a spherical cavity with a radius of ~1.4 Å. If the van der Waals radii of the atoms are taken into account, the cavity radius would be ~2.1 Å [73]. Thus, the HCOF molecule could fit in a volume of one hard-sphere xenon atom (diameter 4.38 Å) in a solid xenon lattice. In lighter rare gases, however, the cavity diameter is too small to provide trapping in a single substitutional site. In the photodissociation of HCOF, the products are formed in the cage of the parent HCOF molecule with a minor probability for cage exit. This trapping site, if its diameter is taken as ~4.4 Å, is too small for the CO···HF and OC···HF complexes. According to this assumption, distorted structures of CO···HF and OC···HF are expected. This is consistent with the annealing experiments of UV-irradiated HCOF/Rg samples in Paper III. The sum of the bond lengths and van der Waals radii gives radii (or "effective lengths") of 5.8 Å and 5.9 Å for the CO···HF and OC···HF complexes, respectively. In order to fit into a spherical cavity with a diameter of 4.4 Å, a 1.4 Å shortening of their "effective length" would be needed. If this shortening is assumed to take place by a contraction of the intermolecular bond, the excitation energy would be decreased by ~0.8 eV. In this picture the H–F and C–O bond lengths are kept constant, which may lead to a qualitatively and quantitatively wrong description of the system. In a small cavity the intramolecular bond lengths may be distorted by the perturbation induced by nearby molecules and the dimensions of the CO···HF and OC···HF complexes could be relatively far from their equilibrium structures.

Chapter 4

Conclusions

The photochemistry of small molecules embedded in solid rare gas matrices is studied in this thesis. The main focus has been on the photodissociation of hydrogen halides and the subsequent thermally induced reactions of hydrogen atoms, as well on the spectroscopy and photochemistry of formyl fluoride in argon, krypton, and xenon matrices. The main interest of this thesis is to contribute to the understanding of the chemistry of the solid environment at the molecular level..

The electronic absorption spectra of HXeH, HXeCl, HXeBr, HXeI, HXeCN, HXeSH, and HXeOH were recorded in a xenon matrix. All these compounds have broad and structureless absorptions in the ultraviolet region. The efficient UV photodecomposition of the rare gas compounds can be regarded as evidence that these transitions are from a bound electronic ground state to repulsive excited states. Since rare gas molecules exhibit significant charge transfer nature in their electronic ground states, the electronic transitions possess charge transfer character. Consistent with this, very large transition dipole moments were computationally estimated for HXeCl, HXeBr, and HXeI. The charge transfer character of these transitions is consistent with the production of the neutral decomposition products.

The thermally induced reactions of hydrogen atoms were studied in more detail in a H_2S/Xe matrix. Since the HXeY molecules are efficient hydrogen atom trapping sites, the thermally induced reactions $H + SH \rightarrow H_2S$ and $H + H \rightarrow H_2$ were only minor loss channels for the thermally mobilised hydrogen atoms in solid xenon. The kinetic model used predicts very small yields of H_2S and H_2, and the experimental data showed even smaller yields. This can be summarised by stating that the role of the solid xenon environment on the $H + H \rightarrow H_2$ and $H + Y \rightarrow HY$ reactions is crucial, and there is a high energy barrier the preventing formation of these reaction products. Similarly, the reaction between a hydrogen atom and $SH \cdots H_2S$ is not

likely to yield an H_2S dimer, as might be expected. Quantum chemical calculations were used to estimate the stability of the $HXeSH\cdots H_2S$ complex. This molecular complex was computationally stable, and it could thus be the product of the $H + SH\cdots H_2S$ reaction in solid xenon. However, this was not unambiguously supported by spectral observations.

The photodissociation of formyl fluoride was studied in argon, krypon, and xenon matrices. Since the photon energies used were below the threshold for cage exit of hydrogen and fluorine atoms produced in photodissociation, the photochemical products were mainly complexes between CO and HF due to in-cage reactions $H + FCO \rightarrow HF + CO$ and $F + HCO \rightarrow HF + CO$. Only minor evidence of atomic cage exit was observed in krypton and xenon matrices. An interesting observation was the photodissociation of CO/HF complexes in krypton and xenon matrices, because both CO and HF have their first excited states inaccessible to the photon energies used. Isolated CO and HF were both stable with respect to UV irradiation in solid krypton.

The vertical excitation energies of the $CO\cdots HF$ and $OC\cdots HF$ complexes in their ground state geometries were estimated by quantum chemical calculations. These calculations showed that the electronic states of molecular fragments are only slightly perturbed by complex formation, and thus the computed transitions were almost pure molecular transitions and inaccessible by the photon energies used. However, experimental observations showed that the photodissocation of HCOF mostly yielded $CO\cdots HF$ and $OC\cdots HF$ complexes in their non-relaxed geometries. Some estimates were provided for the cavity size of the complexes by using the van der Waal radius of the HCOF molecule as the cavity radius. To fit in this cavity, the lengths of the $CO\cdots HF$ complexes were significantly reduced. A 1.4 Å shortening of the intermolecular distance decreased the CIS transition energy by 0.8 eV, which would suggest that the non-relaxed structures may have lower excitation energies. However, photodissociation was observed only in krypton and xenon matrices, where the photodissociation was more efficient. This would imply some role of the surrounding rare gas atoms as well.

Low-temperature trapping of molecular complexes was used in the spectroscopical study of the HCOF dimers. In this study a band ca. 17 cm^{-1} blue-shifted from the monomer C–H stretching fundamental was assigned to the C–H stretching fundamental of the $-C-H\cdots O-$ hydrogen bond. Quantum chemical calculations showed that the dimer structure containing double $-C-H\cdots O-$ hydrogen bonds is probably the most abundant dimer in matrices. This was supported by the energetics and harmonic vibrational analysis of different dimer structures.

As a summary, a solid surrounding has substantial effects on chemical reactions. For example, the gas phase reaction $H + H \rightarrow H_2$ is not favored

in solid xenon, where HXeH is the main reaction product. The cage effect prevents atomic cage exits and thus subsequent in-cage reactions of photoproducts may lead to qualitatively and quantitatively different final products. Despite their conceptual inertness, rare gases have diverse effects on chemical events.

Bibliography

[1] E. Whittle, D. A. Dows, and G. C. Pimentel, J. Chem. Phys. **22**, 1943 (1954).

[2] I. R. Dunkin, *Matrix-Isolation Techniques. A Practical Approach.* (Oxford University Press, 1998).

[3] H. E. Hallam, ed., *Vibrational Spectroscopy of Trapped Species* (John Wiley & Sons, 1973).

[4] W. Weltner, Jr, *Magnetic Atoms and Molecules* (Dover Publication, Inc., 1989).

[5] A. J. Barnes and W. J. Orville-Thomas, eds., *Vibrational Spectroscopy – Modern trends* (Elsevier, 1977).

[6] H. Sato, Chem. Rev. **101**, 2687 (2001).

[7] V. A. Apkarian and N. Schwentner, Chem. Rev. **99**, 1481 (1999).

[8] W. G. Lawrence and V. A. Apkarian, J. Chem. Phys. **97**, 6199 (1992).

[9] M. E. Fajardo and V. A. Apkarian, J. Chem. Phys. **85**, 5660 (1986).

[10] M. E. Fajardo and V. A. Apkarian, J. Chem. Phys. **89**, 4102 (1988).

[11] M. E. Fajardo and V. A. Apkarian, J. Chem. Phys. **89**, 4124 (1988).

[12] M. S. Gudipati, J. Phys. Chem. A **101**, 2003 (1997), and references therein.

[13] V. E. Bondybey, M. Räsänen, and A. Lammers, Annu. Rep. Prog. Chem., Sect. C **95**, 331 (1999).

[14] R. Schriever, M. Chergui, H. Kunz, and N. Schwentner, J. Chem. Phys. **91**, 4128 (1989).

[15] R. Schriever, M. Chergui, Ö. Ünal, and N. Schwentner, J. Chem. Phys. **93**, 6124 (1990).

[16] R. Schriever, M. Chergui, and N. Schwentner, J. Phys. Chem. **95**, 6124 (1991).

[17] K. O. Christe, Angew. Chem. Int. Ed. **40**, 1419 (2001).

[18] N. Bartlett, Proc. Chem. Soc., 218 (1962).

[19] F. O. Saldky, P. A. Bulliner, and N. Bartlett, J. Chem. Soc. A: Inorg. Phys. Theor., 2179 (1969).

[20] M. Pettersson, J. Lundell, and M. Räsänen, Eur. J. Inorg. Chem., 729 (1999).

[21] R. B. Gerber, Ann. Rev. Phys. Chem., 55 (2004).

[22] M. Pettersson, L. Kriachtchev, J. Lundell, and M. Räsänen, *Inorganic Chemistry in Focus II* (Wiley–VCH, 2005), chap. Noble gas hybride compounds.

[23] M. Pettersson, J. Lundell, and M. Räsänen, J. Chem. Phys. **102**, 6423 (1995).

[24] M. Pettersson, J. Lundell, L. Khriachtchev, and M. Räsänen, J. Chem. Phys. **109**, 618 (1998).

[25] M. Pettersson, J. Lundell, L. Khriachtchev, E. Isoniemi, and M. Räsänen, J. Am. Chem. Soc. **120**, 7979 (1998).

[26] M. Pettersson, L. Khriachtchev, J. Lundell, and M. Räsänen, J. Am. Chem. Soc. **121**, 11904 (1999).

[27] M. Pettersson, J. Lundell, and M. Räsänen, J. Chem. Phys. **103**, 205 (1995).

[28] L. Khriachtchev, H. Tanskanen, J. Lundell, M. Pettersson, H. Kiljunen, and M. Räsänen, J. Am. Chem. Soc. **125**, 4696 (2003).

[29] L. Khriachtchev, M. Pettersson, N. Runeberg, J. Lundell, and M. Räsänen, Nature **406**, 874 (2000).

[30] M. W. Wong, J. Am. Chem. Soc. **122**, 6289 (2000).

[31] G. M. Chaban, J. Lundell, and R. B. Gerber, J. Chem. Phys. **115**, 7341 (2001).

[32] T. Takayanagi and A. Wada, Chem. Phys. Lett. **352**, 91 (2002).

[33] Z. Bihary, G. M. Chaban, and R. B. Gerber, J. Chem. Phys. **117**, 5105 (2002).

[34] A. Lignell, L. Khriachtchev, M. Räsänen, and M. Pettersson, Chem. Phys. Lett. **390**, 256 (2004).

[35] H. Muto, K. Nunome, and M. Iwasaki, J. Phys. Chem. **84**, 3402 (1980).

[36] D. L. E. Weitz, Chem. Phys. Lett. **211**, 430 (1993).

[37] D. LaBrake, E. T. Ryan, and E. Weitz, J. Chem. Phys. **102**, 4112 (1995).

[38] F. Wittl, J. Eberlein, T. Epple, M. Dechant, and M. Creuzburg, J. Chem. Phys. **98**, 9554 (1993).

[39] J. Eberlein and M. Creuzburg, J. Chem. Phys. **106**, 2188 (1997).

[40] I. Last and T. F. George, J. Chem. Phys. **89**, 3071 (1988).

[41] N. Runeberg, M. Seth, and P. Pyykkö, Chem. Phys. Lett. **246**, 239 (1995).

[42] G. A. Jeffrey, *An Introduction to Hydrogen Bonding* (Oxford University Press, 1997).

[43] H. Umeyama and K. Morokuma, J. Am. Chem. Soc. **99**, 1316 (1977).

[44] P. Hobza and Z. Havlas, Chem. Rev. **100**, 4253 (2000).

[45] S. Scheiner and T. Kar, J. Phys. Chem. A **106**, 1784 (2002).

[46] A. J. Barnes, J. Mol. Struct. **704**, 3 (2004).

[47] M. J. Frisch, G. W. Trucks, H. B. Schlegel, G. E. Scuseria, M. A. Robb, J. R. Cheeseman , Montgomery, Jr., J. A., T. Vreven, K. N. Kudin, J. C. Burant, J. M. Millam, S. S. Iyengar, J. Tomasi, V. Barone, B. Mennucci, M. Cossi, G. Scalmani, N. Rega , G. A. Petersson, H. Nakatsuji, M. Hada, M. Ehara, K. Toyota, R. Fukuda, J. Hasegawa , M. Ishida, T. Nakajima, Y. Honda, O. Kitao, H. Nakai, M. Klene, X. Li, J. E. Knox, H. P. Hratchian, J. B. Cross, V. Bakken, C. Adamo, J. Jaramillo, R. Gomperts, R. E. Stratmann, O. Yazyev, A. J. Austin, R. Cammi,

C. Pomelli, J. W. Ochterski, P. Y. Ayala, K. Morokuma, G. A. Voth, P. Salvador, J. J. Dannenberg, V. G. Zakrzewski, S. Dapprich, A. D. Daniels , M. C. Strain, O. Farkas, D. K. Malick, A. D. Rabuck, K. Raghavachari, J. B. Foresman , J. V. Ortiz, Q. Cui, A. G. Baboul, S. Clifford, J. Cioslowski, B. B. Stefanov, G. Liu, A. Liashenko, P. Piskorz, I. Komaromi, R. L. Martin, D. J. Fox, T. Keith, M. A. Al-Laham, C. Y. Peng, A. Nanayakkara, M. Challacombe, P. M. W. Gill , B. Johnson, W. Chen, M. W. Wong, C. Gonzalez and J. A. Pople, Gaussian 03, Revision C.02, Gaussian, Inc., Wallingford, CT, 2004.

[48] MOLPRO is a package of ab initio programs written by H.-J. Werner and P. J. Knowles and R. Lindh and M. Schütz and P. Celani and T. Korona and F. R. Manby and G. Rauhut and R. D. Amos and A. Bernhardsson and A. Berning and D. L. Cooper and M. J. O. Deegan and A. J. Dobbyn and F. Eckert and C. Hampel and G. Hetzer and A. W. Lloyd and S. J. McNicholas and W. Meyer and M. E. Mura and A. Nicklass and P. Palmieri and R. Pitzer and U. Schumann and H. Stoll and A. J. Stone and R. Tarroni and T. Thorsteinsson, see http://www.molpro.net.

[49] "GAMESS – **G**eneral **A**tomic and **M**olecular **E**lectronic **S**tructure **S**ystem."
M. W. Schmidt, K. K. Baldridge , J. A. Boatz, S. T. Elbert, M. S. Gordon, J. H. Jensen, S. Koseki, N. Matsunaga, K. A. Nguyen, S. Su, T. L. Windus, M. Dupuis and J. A. Montgomery, J. Comput. Chem. **14**, 1347 (1993), see http://www.msg.ameslab.gov/GAMESS/.

[50] P. W. Atkins and R. S. Friedman, *Molecular Quantum Meachanics* (Oxford University Press, 1997).

[51] F. Jensen, *Introduction to Computational Chemistry* (John Wiley & Sons, 1999).

[52] J. F. Stanton and R. J. Bartlett, J. Chem. Phys. **98**, 7029 (1993).

[53] M. A. L. Marques and E. K. U. Gross, Annu. Rev. Phys. Chem. **55**, 427 (2004).

[54] K. Raghavachari and J. B. Anderson, J. Phys. Chem. **100**, 12960 (1996).

[55] R. Krishnan, J. S. Binkley, R. Seeger, and J. A. Pople, J. Chem. Phys. **72**, 650 (1980).

[56] T. Clark, J. Chandrasekhar, and P. v. R. Schleyer, J. Comp. Chem **4**, 294 (1983).

[57] Basis sets were obtained from the Extensible Computational Chemistry Environment Basis Set Database, Version 02/25/04, as developed and distributed by the Molecular Science Computing Facility, Environmental and Molecular Sciences Laboratory which is part of the Pacific Northwest Laboratory, P.O. Box 999, Richland, Washington 99352, USA, and funded by the U.S. Department of Energy. The Pacific Northwest Laboratory is a multi-program laboratory operated by Battelle Memorial Institute for the U.S. Department of Energy under contract DE-AC06-76RLO 1830. Contact Karen Schuchardt for further information.

[58] T. H. Dunning, Jr., J. Chem. Phys. **90**, 1007 (1989).

[59] A. Nicklass, M. Dolg, H. Stoll, and H. Preuss, J. Chem. Phys. **102**, 8942 (1995).

[60] G. Igel-Mann, H. Stoll, and H. Preuss, Mol. Phys. **65**, 1321 (1988).

[61] A. Bergner, A. Dolg, W. Kuchle, H. Stoll, and H. Preuss, Mol. Phys. **80**, 1431 (1993).

[62] M. Creuzburg, F. Koch, and F. Wittl, Chem. Phys. Lett. **156**, 387 (1989).

[63] M. Kraas and P. Gürtler, Chem. Phys. Lett. **174**, 396 (1990).

[64] V. I. Frldman, F. F. Sukhov, and A. Y. Orlov, Chem. Phys. Lett. **280**, 507 (1997).

[65] M. Pettersson, J. Nieminen, L. Khriachtchev, and M. Räsänen, J. Chem. Phys. **107**, 8423 (1997).

[66] L. Khriachtchev, M. Pettersson, H. Tanskanen, and M. Räsänen, Chem. Phys. Lett. **359**, 135 (2002).

[67] L. Khriachtchev, H. Tanskanen, M. Pettersson, M. Räsäenen, J. Ahokas, H. Kunttu, and V. Feldmann, J. Chem. Phys. **116**, 5649 (2002).

[68] S. L. Fiedler, K. Vaskonen, J. Ahokas, H. Kunttu, J. Eloranta, and V. A. Apkarian, J. Chem. Phys. **117**, 8867 (2002).

[69] J. Goodman and L. E. Brus, J. Chem. Phys. **67**, 4858 (1977).

[70] E. T. Ryan and E. Weitz, J. Chem. Phys. **99**, 1004 (1993).

[71] S. Tanaka, H. Kajihara, S. Koda, and V. A. Apkarian, Chem. Phys. Lett. **233**, 555 (1995).

[72] M. S. Gudipati and A. Klein, Chem. Phys. Lett. **344**, 479 (2001).

[73] *CRC, Handbook of Chemistry and Physics, 57th edition*, CRC Press (1976).

[74] B. K. Janousek and J. I. Brauman, Phys. Rev. A **23**, 1673 (1981).

[75] S. E. Bradforth, E. H. Kim, D. W. Arnold, and D. M. Neumark, J. Chem. Phys. **98**, 800 (1993).

[76] R. G. Mortimer, *Physical Chemistry* (Harcourt Academic Press, 2000).

[77] A. Lignell, L. Kriachtchev, M. Pettersson, and M. Räsänen, J. Chem. Phys. **117**, 961 (2002).

[78] A. Lignell, L. Kriachtchev, M. Pettersson, and M. Räsänen, J. Chem. Phys. **118**, 11120 (200).

[79] A. V. Nemukhin, B. L. Grigorenko, L. Khriachtchev, H. Tanskanen, M. Pettersson, and M. Räsänen, J. Am. Chem. Soc. **124**, 10706 (2002).

[80] J. Lundell and M. Pettersson, Phys. Chem. Chem. Phys. **1**, 1691 (1999).

[81] S. A. C. McDowell, Chem. Phys. Lett. **368**, 649 (2003).

[82] S. A. C. McDowell, Phys. Chem. Chem. Phys. **5**, 808 (2003).

[83] E. Isoniemi, M. Pettersson, L. Khriachtchev, J. Lundell, and M. Räsänen, J. Phys. Chem. A **103**, 679 (1999).

[84] D. E. Woon and T. H. Dunning, Jr., J. Chem. Phys. **98**, 1358 (1993).

[85] G. Shatte, H. Willner, D. Hoge, E. Knözinger, and O. Schrems, J. Phys. Chem. **93**, 6025 (1989).

[86] A. Kovács, A. Szabó, D. Nemchok, and I. Hargittai, J. Phys. Chem. A **106**, 5671 (2002).

[87] S. F. Boys and F. Bernardi, Mol. Phys. **19**, 553 (1970).

[88] J. J. Novoa, M. Planas, and M. C. Rovira, Chem. Phys. Lett. **251**, 33 (1996).

[89] D. E. Klimek and M. J. Berry, Chem. Phys. Lett. **21**, 141 (1973).

[90] Y. S. Choi and C. B. Moore, J. Chem. Phys. **97**, 1010 (1992).

[91] B. R. Weiner and R. N. Rosenfeld, J. Phys. Chem. **92**, 4640 (1988).

[92] C. Maul, C. Dietrich, T. Haas, K.-H. Gericke, H. Tachikawa, S. R. Langford, M. Kono, C. L. Reed, R. N. Dixon, and M. N. R. Ashfold, Phys. Chem. Chem. Phys. **1**, 767 (1999).

[93] C. L. Reed, M. Kono, S. R. Langford, W. R. Hancock, R. N. Dixon, and M. N. R. Ashfold, J. Chem. Soc., Faraday Trans. **93**, 2721 (1997).

[94] C. L. Reed, M. Kono, S. R. Langford, W. R. Hancock, R. N. Dixon, and M. N. R. Ashfold, J. Chem. Phys. **106**, 6198 (1997).

[95] T. W. R. Hancock and R. N. Dixon, J. Chem. Soc., Faraday Trans. **93**, 2707 (1997).

[96] S.-H. Lee, C.-Y. Wu, S.-K. Yang, and Y.-P. Lee, J. Chem. Phys. **123**, 074326 (2005).

[97] W.-H. Wang and R.-Z. Liu, J. Chem. Phys. **115**, 5411 (2001).

[98] L. E. Giddings, Jr. and K. K. Innes, J. Mol. Spectrosc. **6**, 528 (1961).

[99] H. Y. Afeefy, J. F. Liebman and S. E. Stein "Constants of Diatomic Molecules" by K.P. Huber and G. Herzberg (data prepared by J.W. Gallagher and R.D. Johnson, III) in **NIST Chemistry WebBook, NIST Standard Reference Database Number 69**, Eds. P. J. Linstrom and W. G. Mallard, June 2005, National Institute of Standards and Technology, Gaithersburg MD, 20899 (http://webbook.nist.gov).

Paper I

https://doi.org/10.1021/jp002141t

Paper II

https://doi.org/10.1021/jp0259824

Paper III

https://doi.org/10.1021/jp060249o

Paper IV

https://doi.org/10.1021/jp061188x